The Astrophysical Journal Supplement Series, 279:35 (27pp), 2025 August https://doi.org/10.3847/1538-4365/ade0ad

The Karl G. Jansky Very Large Array Local Group *L*-Band Survey (LGLBS)

Eric W. Koch[1,2], Adam K. Leroy[3,4], Erik W. Rosolowsky[5], Laura Chomiuk[6], Julianne J. Dalcanton[7,8], Nickolas M. Pingel[9], Sumit K. Sarbadhicary[3,4,10], Snežana Stanimirović[9], Fabian Walter[11], Haylee N. Archer[12,13], Alberto D. Bolatto[14], Michael P. Busch[15], Hongxing Chen[9], Ryan Chown[3], Harrisen Corbould[5], Serena A. Cronin[16], Jeremy Darling[17], Thomas Do[6], Jennifer Donovan Meyer[18], Cosima Eibensteiner[18,33], Deidre Hunter[13], Rémy Indebetouw[18,19], Preshanth Jagannathan[20], Amanda A. Kepley[18], Chang-Goo Kim[21], Shin-Jeong Kim[22], Timea O. Kovacs[11], Joshua Marvil[20], Eric J. Murphy[18], Claire E. Murray[23,24], Jürgen Ott[20], D.J. Pisano[25], Mary Putman[26], Daniel R. Rybarczyk[9], Julia Roman-Duval[23], Karin Sandstrom[15], Eva Schinnerer[11], Evan D. Skillman[27], Adam Smercina[23,32], Ioana Stelea[9], Jay Strader[6], Jiayi Sun[21,32], Devisree Tallapaneni[3], Elizabeth Tarantino[23], Vicente Villanueva[28], Daniel R. Weisz[29], Thomas G. Williams[30], and Tony Wong[31]

[1] Center for Astrophysics | Harvard & Smithsonian, 60 Garden Street, 02138 Cambridge, MA, USA; koch.eric.w@gmail.com
[2] National Radio Astronomy Observatory, 800 Bradbury SE, Suite 235, Albuquerque, NM 87106, USA
[3] Department of Astronomy, The Ohio State University, 140 West 18th Avenue, Columbus, OH 43210, USA
[4] Center for Cosmology and Astroparticle Physics (CCAPP), 191 West Woodruff Avenue, Columbus, OH 43210, USA
[5] Department of Physics, University of Alberta, 4-183 CCIS, Edmonton, Alberta, T6G 2E1, Canada
[6] Center for Data Intensive and Time Domain Astronomy, Department of Physics and Astronomy, Michigan State University, East Lansing, MI 48824, USA
[7] Center for Computational Astrophysics, Flatiron Institute, 162 Fifth Avenue, New York, NY 10010, USA
[8] Department of Astronomy, Box 351580, University of Washington, Seattle, WA 98195, USA
[9] University of Wisconsin–Madison, Department of Astronomy, 475 N Charter Street, Madison, WI 53703, USA
[10] Department of Physics and Astronomy, The Johns Hopkins University, Baltimore, MD 21218, USA
[11] Max-Planck-Institut für Astronomie, Königstuhl 17, 69117 Heidelberg, Germany
[12] School of Earth and Space Exploration, Arizona State University, Tempe, AZ 85287, USA
[13] Lowell Observatory, 1400 W Mars Hill Road, Flagstaff, AZ 86001, USA
[14] Department of Astronomy and Joint Space-Science Institute, University of Maryland, College Park, MD 20854, USA
[15] Department of Astronomy & Astrophysics, University of California, San Diego, 9500 Gilman Drive, La Jolla, CA 92093, USA
[16] Department of Astronomy, University of Maryland, College Park, MD 20854, USA
[17] Center for Astrophysics and Space Astronomy, Department of Astrophysical and Planetary Sciences, University of Colorado, 389 UCB, Boulder, CO 80309, USA
[18] National Radio Astronomy Observatory, 520 Edgemont Road, Charlottesville, VA 22903, USA
[19] University of Virginia Astronomy Department, P.O. Box 400325, Charlottesville, VA, 22904, USA
[20] National Radio Astronomy Observatory, 1011 Lopezville Road, Socorro, NM 87801, USA
[21] Department of Astrophysical Sciences, Princeton University, 4 Ivy Lane, Princeton, NJ 08544, USA
[22] Research School of Astronomy and Astrophysics, The Australian National University, Canberra ACT 2611, Australia
[23] Space Telescope Science Institute, 3700 San Martin Drive, Baltimore, MD 21218, USA
[24] The William H. Miller III Department of Physics & Astronomy, Bloomberg Center for Physics and Astronomy, Johns Hopkins University, 3400 N. Charles Street, Baltimore, MD 21218, USA
[25] Department of Astronomy, University of Cape Town, Private Bag X3, Rondebosch 7701, South Africa
[26] Department of Astronomy, Columbia University, New York, NY 10027, USA
[27] Minnesota Institute for Astrophysics, University of Minnesota, Minneapolis, MN 55455, USA
[28] Departamento de Astronomía, Universidad de Concepción, Barrio Universitario, Concepción, Chile
[29] Department of Astronomy, University of California, Berkeley, Berkeley, CA 94720, USA
[30] Subdepartment of Astrophysics, Department of Physics, University of Oxford, Keble Road, Oxford OX1 3RH, UK
[31] Department of Astronomy, University of Illinois, Urbana, IL 61801, USA
Received 2025 January 31; revised 2025 May 27; accepted 2025 May 28; published 2025 July 17

Abstract

We present the Local Group *L*-Band Survey, a Karl G. Jansky Very Large Array (VLA) survey producing the highest-quality 21 cm and 1–2 GHz radio continuum images to date, for the six VLA-accessible, star-forming, Local Group galaxies. Leveraging the VLA's spectral multiplexing power, we simultaneously survey the 21 cm line at high 0.4 km s^{-1} velocity resolution, the 1–2 GHz polarized continuum, and four OH lines. For the massive spiral M31, the dwarf spiral M33, and the dwarf irregular galaxies NGC 6822, IC 10, IC 1613, and the Wolf–Lundmark–Melotte Galaxy, we use all four VLA configurations and the Green Bank Telescope to reach angular resolutions of $<5''$ (10–20 pc) for the 21 cm line with $<10^{20}$ cm^{-2} column density sensitivity, and even sharper views ($<2''$; 5–10 pc) of the continuum. Targeting these nearby galaxies ($D \lesssim 1$ Mpc) reveals a sharp, resolved view of the atomic gas, including 21 cm absorption, and continuum emission from supernova remnants and H II regions. These data sets can be used to test theories of the abundance and formation of cold clouds, the driving and dissipation of interstellar turbulence, and the impact of feedback from massive stars and supernovae. Here, we

[32] Jansky Fellow of the National Radio Astronomy Observatory.
[33] Hubble Fellow.

describe the survey design and execution, scientific motivation, data processing, and quality assurance. We provide a first look at and publicly release the wide-field 21 cm H I data products for M31, M33, and four dwarf irregular targets in the survey, which represent some of the highest-physical-resolution 21 cm observations of any external galaxies beyond the LMC and SMC.

Unified Astronomy Thesaurus concepts: Local Group (929); Andromeda Galaxy (39); Triangulum Galaxy (1712); Interstellar medium (847); Radio interferometry (1346)

1. Introduction

Atomic gas (H I) makes up most of the interstellar medium (ISM) in most galaxies at all redshifts, and represents a significant majority of the gas in the disks of galaxies at $z = 0$ (L. J. Tacconi et al. 2020; F. Walter et al. 2020; A. Saintonge & B. Catinella 2022). The structure of this atomic gas on scales of $\approx 10-100$ pc is shaped by turbulence, stellar feedback, and the combination of thermal and dynamical instabilities that govern the formation and destruction of cold clouds (C. L. Dobbs et al. 2014; N. M. McClure-Griffiths et al. 2023). Meanwhile, the H II regions and supernova remnants (SNRs) represent the two most important sources of stellar feedback sources: young, massive stars and supernova explosions (E. Schinnerer & A. K. Leroy 2024).

The L band (ν = 1–2 GHz) contains key diagnostics of atomic gas, H II regions, and SNRs. The 21 cm hyperfine line of hydrogen (ν = 1420 MHz; H. C. van de Hulst 1945; H. I. Ewen & E. M. Purcell 1951) traces the mass, motions, and (combining extinction and absorption) temperature of the atomic ISM (F. J. Kerr et al. 1954; G. B. Field 1958). Meanwhile, the 1–2 GHz radio emission suffers no extinction due to dust, and so offers a direct view of H II regions via free–free emission and SNRs via synchrotron emission, capturing key stages of the life and death of massive stars. Beyond these tracers, the L band also hosts a suite of other, fainter features that access other aspects of the matter cycle. These include diffuse synchrotron and free–free emission, molecular OH transitions at 1612, 1665, 1667, and 1712 MHz, radio recombination lines, and polarization of the continuum.

Unfortunately, the relatively coarse angular resolution of current radio interferometers when configured to achieve the required surface brightness sensitivity has limited our ability to utilize these diagnostics at high physical resolution. Current facilities can observe 21 cm emission at $\sim 5''$ and 1–2 GHz continuum at $\sim 2''$. This is significantly coarser than the $0\farcs1$–$1''$ regularly achieved by facilities studying other phases the ISM, including the Atacama Large Millimeter/submillimeter Array (ALMA) and the James Webb Space Telescope (JWST). This situation is expected to change with the construction of a next-generation Very Large Array (ngVLA; E. J. Murphy et al. 2018) and the Square Kilometre Array (SKA; R. Braun et al. 2015). Until then, matching the $\gtrsim 2''$–$5''$ angular scales accessible to L-band radio facilities to the small physical scales of individual gas clouds, SNRs, or H II regions requires targeting the nearest galaxies.

Galaxies in the Local Group, with $D < 1.2$ Mpc (S. van den Bergh 1999), represent key targets that maximize the physical resolution and mass or luminosity sensitivity of any observations. These galaxies thus offer the best opportunity to detect and resolve individual gas clouds, SNRs, and H II regions, in full context. Because of their proximity, these targets tend to be observed in detail by almost all astronomical facilities, and have seen major investment by facilities from the Hubble Space Telescope (HST; e.g., J. J. Dalcanton et al. 2012; B. F. Williams et al. 2021) and ALMA (e.g., M. Rubio et al. 2015; A. Schruba et al. 2017) to Euclid (e.g., L. K. Hunt et al. 2025) and JWST (e.g., O. C. Jones et al. 2023; J. Peltonen et al. 2024; D. R. Weisz et al. 2024).

Motivated by these considerations, we present the Local Group L-Band Survey (LGLBS), a Karl G. Jansky Very Large Array (VLA) survey designed to address open questions related to the physics of atomic gas, star formation, cosmic rays, and stellar feedback, and to provide a suite of legacy data products. LGLBS targets the six northern, VLA-accessible star-forming Local Group galaxies using all four of the VLA's main configurations (A, B, C, and D, from most extended to compact), and includes short-spacing corrections from the Robert C. Byrd Green Bank Telescope (GBT) for the atomic gas maps. Fortunately, the VLA-accessible Local Group galaxies targeted by LGLBS span a diverse set of physical conditions. M31 (Andromeda) offers us an external view of a close cousin to the Milky Way, M33 (Triangulum) often acts as the prototype dwarf spiral galaxy, and four actively star-forming dwarf irregular galaxies provide windows into the common phenomenon of H I–dominated, star-forming, low-metallicity dwarf galaxies.

The LGLBS project is intended as both a high-detail successor to the successful VLA 21 cm surveys THINGS, LITTLE THINGS, and VLA-ANGST (F. Walter et al. 2008; D. A. Hunter et al. 2012; J. Ott et al. 2012), as well as a preview of the type of observations that the ngVLA and SKA will be able to produce for more distant targets. Most importantly, the project aims to produce sharp views of the atomic gas and radio continuum that develop our understanding of several important but less-studied aspects of the matter cycle in galaxies. We also aim to provide widely useful public data products for this well-studied set of nearest galaxies.

This paper describes the LGLBS science drivers (Section 2), targets (Section 3), observing strategy (Section 4), and data reduction and quality assurance procedures (Section 5). As a demonstration of the results, we present 21 cm H I imaging using the VLA C and D configurations (hereafter CD) (Section 6). Companion papers will detail the full A, B, C, and D (ABCD) configuration 21 cm imaging (N. Pingel et al. 2025, in preparation) and radio continuum imaging (S. Sarbadhicary et al. 2025, in preparation).

2. Scientific Motivation

At $z = 0$, atomic hydrogen (H I) makes up the majority of neutral gas in the Universe, with ~ 3 times more H I than H_2 in galaxies (C. L. Carilli & F. Walter 2013; A. Saintonge & B. Catinella 2022). H I represents the material for molecule and cloud formation, and the ability to convert atomic to molecular gas regulates star formation in many cases (A. K. Leroy et al. 2008; D. A. Hunter et al. 2024). The H I also bears the brunt of much of the stellar feedback in galaxies, from photoelectric heating to supernova feedback. This leads

to important phenomena including fountains, outflows, the carving of shells and holes, and the driving of interstellar turbulence (B. G. Elmegreen et al. 2002; B. G. Elmegreen & J. Scalo 2004; M.-M. Mac Low & R. S. Klessen 2004; R. Sancisi et al. 2008; F. Fraternali 2017; T. A. Thompson & T. M. Heckman 2024). These phenomena affect and are driven by the physical state of the gas, and atomic gas spans a wide range of physical conditions, with densities from $\sim$0.1–100 cm^{-3} and temperatures from $\sim 10^2$–10^4 K (e.g., N. M. McClure-Griffiths et al. 2023). Unlike the mass of atomic gas, the physical state of the H I is not readily accessible from low-resolution 21 cm observations.

LGLBS aims to resolve the 21 cm emission tracing H I down to the scales of individual star-forming regions and ISM clouds ($\sim$25 pc) to diagnose the physical properties of the atomic gas and measure its dynamical and morphological state. Measuring the H I associated with individual molecular-atomic complexes will provide sharp tests of current models used to explain the molecular-to-atomic gas ratio and the rate of star formation in galaxies (e.g., M. R. Krumholz 2014; A. Sternberg et al. 2014; M. G. Wolfire et al. 2022). LGLBS will also allow for identification of atomic gas filaments, bound structures, outflows, shells, and extraplanar atomic gas clouds analogous to the high-velocity clouds seen in the Milky Way. In the Milky Way, such observations have proven critical to assess the role of magnetic fields and turbulence, assess the importance of various instabilities, and study the mechanisms for gas accretion onto the galaxy (see M. E. Putman et al. 2012; C. L. Dobbs et al. 2014; N. M. McClure-Griffiths et al. 2023; A. K. Mittal et al. 2023; A. Hacar et al. 2023). However, so far, this level of detail has been mostly inaccessible in galaxies beyond the Magellanic Clouds.

In addition to high physical resolution, the LGLBS velocity resolution, 0.4 km s^{-1}, is sufficient to resolve thermal line widths for cold $\lesssim$100 K atomic gas. Further, the large areal coverage of the observations and the high angular and velocity resolution allow for searches for 21 cm absorption, not only emission. Paired emission and absorption measurements are a crucial tool for measuring the spin temperature and opacity of the 21 cm line (e.g., C. Heiles & T. H. Troland 2003; C. E. Murray et al. 2014, 2018). Demonstrating this capability, LGLBS has already yielded the first detection of 21 cm absorption in a low-metallicity galaxy (NGC 6822) beyond the Magellanic Clouds (N. M. Pingel et al. 2024).

The inclusion of all VLA configurations and short-spacing GBT data allows LGLBS to recover structure across all scales. As a result, LGLBS will be ideal to study the nature and drivers of interstellar turbulence (e.g., E. W. Koch et al. 2020). The survey meshes naturally with extensive previous investment in these targets. These include massive efforts by HST to map the stellar populations and so capture the sources of stellar feedback (J. A. Holtzman et al. 2006; J. J. Dalcanton et al. 2012; B. F. Williams et al. 2021), efforts by Spitzer and Herschel to map the dust (e.g., B. T. Draine et al. 2014; A. Rémy-Ruyer et al. 2014), and multiple facilities, including ALMA, to observe the molecular gas via the CO lines (e.g., K. Ohta et al. 1993; A. Leroy et al. 2006; C. Nieten et al. 2006; M. Rubio et al. 2015; A. Schruba et al. 2017; K. Muraoka et al. 2023).

In addition to capturing background sources useful for 21 cm absorption studies, the 1–2 GHz radio continuum offers a new view of H II regions and SNRs, tracing recent massive star formation and stellar feedback. Emission in this frequency range is a mixture of free–free and synchrotron emission. The free–free emission provides an extinction-free tracer of the ionizing photon production rate and a probe of H II region structure analogous to hydrogen recombination lines. In the Local Group, our multi-configuration continuum imaging corresponds to $\sim$5–10 pc resolution, sufficient to resolve most evolved H II regions (e.g., L. D. Anderson et al. 2014). Based on the star formation rates of our targets, we expect to measure the free–free emission associated with $\gtrsim$ 5000 optically visible H II regions (e.g., M. Azimlu et al. 2011). Because the free–free emission is unaffected by extinction, LGLBS also offers the opportunity to discover new, embedded regions missed by optical surveys.

The 1–2 GHz continuum also traces SNRs through the synchrotron radiation from shock waves interacting with the ISM, amplifying magnetic fields, and accelerating relativistic particles (e.g., L. Chomiuk & E. M. Wilcots 2009; R. L. White et al. 2019). Radio synchrotron emission from SNRs remains visible for 20–80 kyr, i.e., throughout the ejecta-dominated and Sedov–Taylor phases (e.g., E. G. Berezhko & H. J. Völk 2004). Unlike optical and X-ray diagnostics of SNRs (e.g., J. H. Lee & M. G. Lee 2014; M. Sasaki et al. 2012), radio emission is unaffected by absorption from dust and gas. On more extended scales, the 1–2 GHz synchrotron emission traces cosmic-ray electrons accelerated in SN shocks and diffusing across the galaxy, which acts on large scales as a star formation tracer (e.g., J. J. Condon 1992) but with additional dependence on the magnetic field, ISM density, and aging of the cosmic-ray e^- population.

Beyond mapping the atomic gas, H II regions, and SNRs, the LGLBS spectral setup also captures the polarized radio continuum and line emission from the OH molecule. These tracers are fainter but offer potentially important constraints on ISM conditions. The polarized radio continuum traces the geometry of the magnetic fields and constrains field strength (R. Beck 2015). The OH transitions at 1.612, 1.665, 1.667, and 1.712 GHz offer the prospect to find new OH masers or trace molecular gas, including CO-dark gas, in emission or absorption (e.g., R. J. Allen et al. 1995; M. P. Busch 2024).

These goals mean that LGLBS represents a natural complement to the new GASKAP-HI (N. M. Pingel et al. 2022) and GASKAP-OH (J. R. Dawson et al. 2024) surveys of the Magellanic Clouds and Milky Way and recent investment in emission, absorption, and continuum studies of the Milky Way plane (e.g., GALFA, 21-SPONGE, THOR, and the MeerKAT Galactic Plane Survey; J. E. G. Peek et al. 2011; C. E. Murray et al. 2014; H. Beuther et al. 2016; C. E. Murray et al. 2018; P. V. Padmanabh et al. 2023). Our goal is to expand a similarly detailed view to an external perspective, covering the diverse northern Local Group galaxies.

3. The Local Group Sample

There are eight Local Group ($D < 1.2$ Mpc S. van den Bergh 1999) galaxies with ongoing star formation (i.e., UV or Hα emission) and that are gas rich ($M_{\rm HI} \gtrsim 10^{7.5}\ M_\odot$; I. D. Karachentsev et al. 2004, 2013). LGLBS observes the six of these targets visible to the VLA (decl. $\gtrsim -35°$; Figure 1). These are the massive spiral M31, the dwarf spiral M33, and four dwarf irregulars: IC 10, IC 1613, NGC 6822, and Wolf–Lundmark–Melotte (WLM). The other two galaxies with gas masses $>10^8 M_\odot$ are the LMC and SMC, which are located in the Southern Hemisphere and currently being observed by

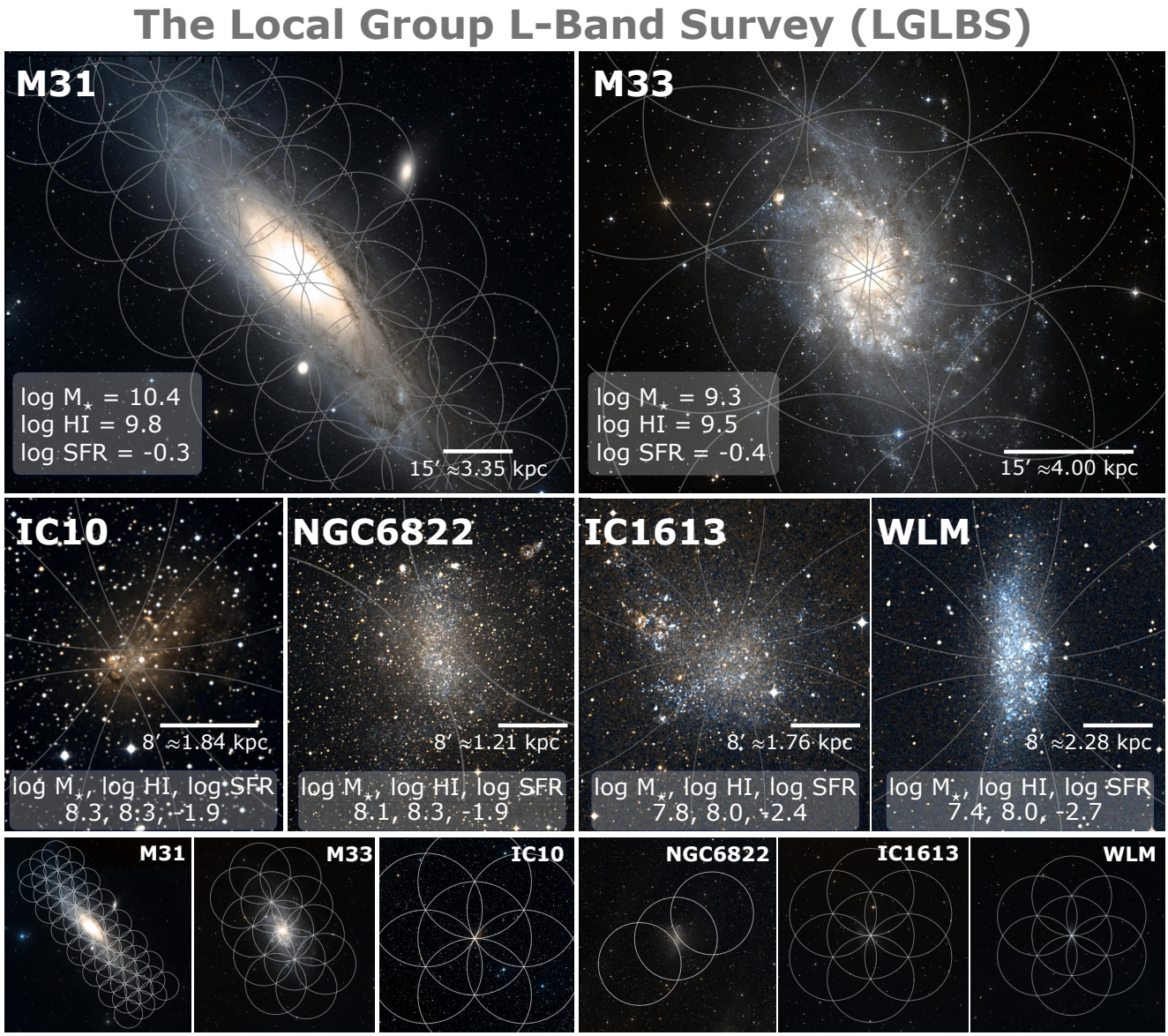

Figure 1. Three-color optical images showing the six Northern Hemisphere local galaxies ordered by decreasing stellar mass (image credits: DESI Legacy Survey; T. M. C. Abbott et al. 2018; E. Morganson et al. 2018; B. Flaugher et al. 2015) overlaid with the VLA pointings. The scale bars on the lower-right corners indicate about one radius (for M31 and M33) and a half of the radius (for IC 10, NGC 6822, IC 1613, and WLM) of one VLA pointing. The lower row shows the full extent of the LGLBS pointings.

SKA precursors (e.g., GASKAP; J. M. Dickey et al. 2013; N. M. Pingel et al. 2022).

Although it remains a small sample, the Local Group captures a large diversity in the conditions relevant to ISM physics, star formation, and galaxy evolution. We summarize the properties of our targets in Table 1, and Figure 2 shows these properties in the broader context of the local galaxy population. M31 is a massive, dust- and metal-rich spiral, with low-intensity star formation, an extended H I disk, and a flat rotation curve (E. Corbelli et al. 2010). While similar in scale to the Milky Way, M31 provides an external perspective on the ISM, star formation, and galactic structure. M33 is a dwarf spiral, comparable in mass and star formation properties to the LMC, but it features a comparatively undisturbed flocculent disk (E. Corbelli 2003). The four low-mass dwarf galaxies (IC 10, IC 1613, NGC 6822, and WLM) have irregular ISM morphologies dominated by extended H I distributions and giant shells, which are driven by stellar feedback (e.g., E. M. Wilcots & B. W. Miller 1998; W. J. G. de Blok & F. Walter 2006; D. A. Hunter et al. 2012; see Table 2 for more references). Compared to the Milky Way and M31, these low-mass dwarf galaxies also have lower dust and metal abundances, by factors of 3–10, solid body or dispersion-dominated kinematics, and extended H I reservoirs (M. L. Mateo 1998; I.-D. Chiang et al. 2021). Our targets overlap the LMC and SMC in stellar mass and metallicity but differ in key ways. Most notably, the recent star formation history and large-scale ISM structure in the LMC and SMC are heavily impacted by ongoing interactions with each other and with the Milky Way halo (S. Stanimirovic et al. 1999; M. E. Putman et al. 2003; G. Besla et al. 2012; Y. C. Joshi et al. 2019; S. Lucchini et al. 2021) while the LGLBS targets are more isolated (M. L. Mateo 1998). The

Table 1
Physical Properties of Targets

Property	IC 10	IC 1613	M31	M33	NGC 6822	WLM
Adopted d (kpc)[a]	770 ± 100[b] [1]	760 ± 36 [2]	776 ± 22 [3]	859 ± 24 [3]	526 ± 25 [2]	984 ± 19 [4]
NED range in d (kpc)[c]	741 ± 85	729 ± 40	780 ± 37	867 ± 67	479 ± 31	958 ± 37
WISE1 $\log_{10}(M_\star/M_\odot)$[d]	8.7	7.8	10.6	9.6	8.1	7.4
Literature $\log_{10}(M_\star/M_\odot)$[d]	7.9 [5]	8.0 [5]	10.85 [6]	9.5 [5]	8.1 [5]	7.7 [5]
$\log_{10}(M_{\rm HI}/M_\odot)$[e]	7.88	7.80	9.80	9.30	8.25	7.91
$\log_{10}[{\rm SFR}/(M_\odot\ \ {\rm yr}^{-1})]$[f]	−1.7	−2.2	−0.4	−0.5	−2.1	−2.4
$12 + \log_{10}{\rm O/H}$[g]	8.37	7.73	8.94	8.59	8.23	7.83
$\frac{d}{dR}\log_{10}{\rm O/H}$ (dex/kpc)[g]	⋯	⋯	−0.024	−0.037	−0.17	⋯

Notes.
[a] Current best-estimated distances. References: [1] F. Dell'Agli et al. (2018), N. Sanna et al. (2008), S. A. N. Gerbrandt et al. (2015), [2] A. J. Lee et al. (2024), [3] A. Savino et al. (2022), [4] A. J. Lee et al. (2021). For reference LITTLE THINGS (D. A. Hunter et al. 2012) adopted distances of 0.7 kpc to IC 10, 0.7 kpc to IC 1613, 0.5 kpc to NGC 6822, and 1.0 to kpc to WLM. A. W. McConnachie (2012) and M. E. Putman et al. (2021) adopted 794 ± 44 to IC 10, 755 ± 42 to IC 1613, 459 ± 17 to NGC 6822, and 933 ± 34 to WLM.
[b] IC 10 has the most uncertain distance among our targets. Our adopted value is from F. Dell'Agli et al. (2018) and intermediate between N. Sanna et al. (2008) and S. A. N. Gerbrandt et al. (2015) and the adopted M. E. Putman et al. (2021) and LITTLE THINGS values. The larger uncertainty reflects our estimate of the scatter among current quality distance estimates.
[c] Median and standard deviation inferred from median absolute deviation for distances compiled by NED (I. Steer et al. 2017) with publication dates between 2000 and the last update of the compilation around 2018.
[d] Stellar mass from integrating median Wide-field Infrared Survey Explorer 1 (WISE1) surface density profiles assuming our adopted distance and mass to light ratio $\Upsilon_\star = 0.5\ L_\odot/M_\odot$. Comparisons to literature values from: [6] J. Yin et al. (2009) (M31) and [5] A. W. McConnachie (2012) (all others). The higher WISE1 mass for IC 10 agrees with Two Micron All Sky Survey results (T. H. Jarrett et al. 2003). $\Upsilon_\star$ may be too low for M31 based on O. G. Telford et al. (2020).
[e] Total H I mass measured, assuming optically thin emission, from the GBT H I cubes with their larger spatial extents and accounting for flux calibration correction factors compared to the LGLBS VLA data. See Section 6 and Appendix B.
[f] Approximate star formation rates estimated from GALEX FUV maps for IC 1613, NGC 6822, and WLM, corrected for Milky Way extinction. Estimated from WISE4 maps for IC 10 and combined GALEX and WISE4 for M31 and M33 following A. K. Leroy et al. (2019).
[g] Metallicities and radial gradients, rescaled for our adopted distances. These assumed values favor T_e-based determinations of metallicities from optical spectroscopy of H II regions. The central value of the metallicity is reported if there is a defined gradient; otherwise, the value reports the average over the observations. IC 10: M. Cosens et al. (2024), IC 1613: F. Bresolin et al. (2007), M31: A. Zurita & F. Bresolin (2012) M33: N. S. J. Rogers et al. (2022), NGC 6822 H. Lee et al. (2006), WLM: H. Lee et al. (2005)

combination of the four LGLBS dwarfs with the SMC also offers a range of perspectives on the structure of low-mass, H I–dominated galaxies, from the nearly edge-on WLM and SMC to the moderately inclined IC 10, IC 1613, and NGC 6822.

Because it targets the Local Group, LGLBS achieves a unique combination of sensitivity and physical resolution. Figure 3 shows the H I column density sensitivity and physical resolution for LGLBS and other recent or ongoing H I surveys of nearby galaxies. The proximity of our targets combined with the deep VLA coverage leads to order-of-magnitude improvements in physical resolution at comparable column density sensitivities. Thus, LGLBS bridges the gap from nearby galaxy H I surveys to studies of the Milky Way and Magellanic Clouds.

Naturally, the LGLBS targets have been studied in detail in H I and radio continuum by previous surveys. In Table 2, we list prior studies that present interferometric radio continuum and spectral line observations of our targets using the L band. This extensive literature has informed the science case for LGLBS, though the current study supersedes these prior works in the combination of sensitivity and resolution.

4. Observing Strategy

Our observations take maximum advantage of the flexible upgraded WIDAR correlator (R. A. Perley et al. 2011; see Section 4.1). We design mosaics that cover the area of known 21 cm emission and active star formation in each of our targets (Section 4.2). Finally, we observe each target in each VLA configuration to provide high resolution while maintaining good surface brightness sensitivity (Section 4.3).

LGLBS (VLA project code 20A-346) builds on several pilot projects (E. W. Koch et al. 2018b, 2020, 2021) that are summarized in Table 4. We integrate these data into our final data products. This pilot work adopted a similar observing strategy as presented here for the full LGLBS survey.

4.1. Spectral Coverage

Figure 4 visualizes our spectral setup. Our observations use this single L-band setup to simultaneously observe:

1. *21 cm H I line.* We use an 8 MHz wide spectral band to cover the 21 cm H I line, observing with dual polarization, 1.95 kHz channel width (0.4 km s^{-1}), and centered at the 1420.405752 MHz rest frequency of the 21 cm transition shifted by the recession velocity of the source given in Table 3. The equivalent bandwidth of 1700 km s^{-1} covers the full velocity extent of each target (Section 3), as well as Milky Way emission along the line of sight, while still allowing for sufficient line-free bandwidth to enable in-band continuum subtraction. The 0.4 km s^{-1} velocity resolution ensures that we can resolve the thermal line profile of a ∼100 K cloud in the cold neutral medium (1σ line width ∼0.9 km s^{-1}).
2. *1–2 GHz continuum.* We use sixteen 64 MHz spectral bands to cover the L-band continuum with 1 MHz channel width and full polarization. Our main science

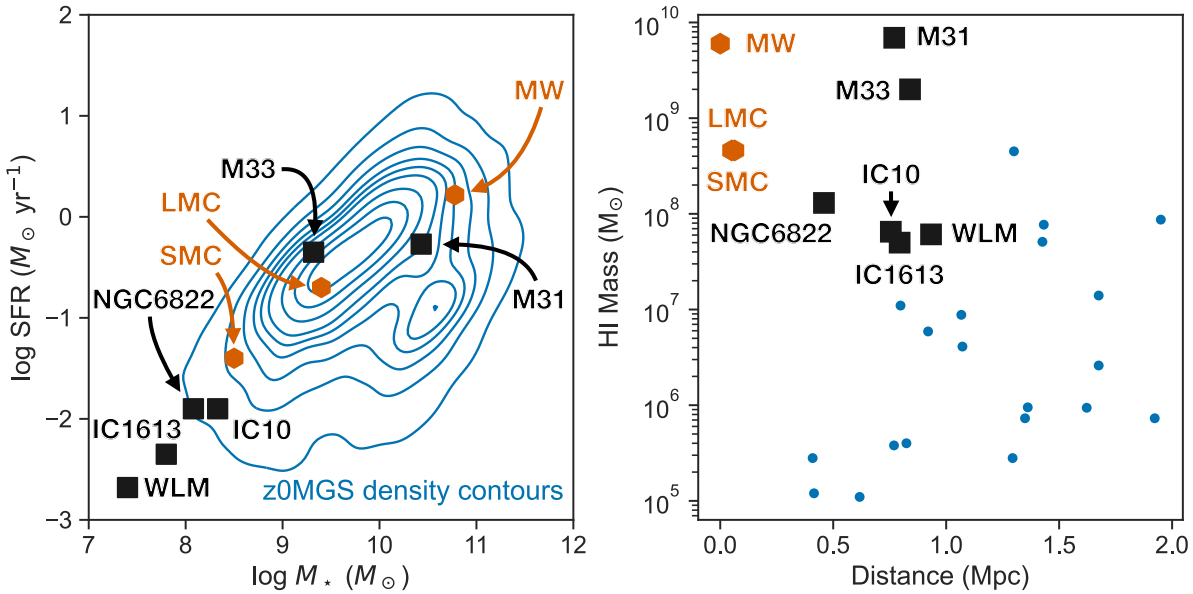

Figure 2. Left panel: star formation rate vs. stellar mass of the LGLBS targets, the SMC, LMC, and Milky Way relative to the local galaxy population ($d < 50$ Mpc) from z0MGS (an archival project combining Wide-field Infrared Survey Explorer (WISE) and GALEX images of nearby galaxies that is complete to $M_\star > 10^9\,M_\odot$; A. K. Leroy et al. 2019). Right panel: H I mass vs. distance for Local Group galaxies with H I detections from the sample compiled in M. E. Putman et al. (2021). The LGLBS H I masses are given in Table 1 from this work. Milky Way values adopted from T. C. Licquia & J. A. Newman (2015) and K. M. Ferrière (2001).

Table 2
Previous High-resolution 21 cm and GHz Radio Continuum Mapping

Galaxy	References
IC 10	H. Yang & E. D. Skillman (1993), E. M. Wilcots & B. W. Miller (1998), G. S. Shostak & E. D. Skillman (1989), B. Namumba et al. (2019), J. Westcott et al. (2017)
IC 1613	G. Lake & E. D. Skillman (1989), T. A. Lozinskaya & N. Y. Podorvanyuk (2009), S. Silich et al. (2006), D. A. Hunter et al. (2012)
M31	E. Brinks & W. W. Shane (1984), R. Braun (1990a), R. Beck et al. (1989), R. Braun (1990b), R. Braun et al. (2009) E. W. Koch et al. (2021)
M33	E. R. Deul & J. M. van der Hulst (1987), D. A. Thilker et al. (2002), F. S. Tabatabaei et al. (2007), E. W. Koch et al. (2018b), S. Z. Kam et al. (2017), R. L. White et al. (2019), F. S. Tabatabaei et al. (2022)
NGC 6822	J. R. Dickel et al. (1985), D. T. F. Weldrake et al. (2003), W. J. G. de Blok & F. Walter (2006), B. Namumba et al. (2017), H.-J. Park et al. (2022)
WLM	D. C. Jackson et al. (2004), A. A. Kepley et al. (2007), D. A. Hunter et al. (2012), R. Ianjamasimanana et al. (2020), Y. Yang et al. (2022)

goals require intensity, Stokes *I*, with both polarizations averaged to minimize noise. We also require the wide bandwidth to achieve our sensitivity goals and to infer the spectral index of continuum emission. The full polarization information provides important information on the magnetic fields in our targets but represents a secondary science goal, with these products expected to follow after our initial analysis. The full polarization information is also potentially helpful for flagging radio frequency interference (RFI). We also place a few backup spectral windows (SPWs) into the line baseband (Baseband A). These were intended to ensure continuum coverage near key lines even in the case of dropped subbands or other correlator glitches. In the end, such problems were extremely rare and these backup bands saw little use.

3. *OH 1612, 1665, 1667, 1720 MHz.* We observe the OH lines at 1612, 1665, 1667, and 1720 MHz. We observe the 1612 and 1720 MHz lines using 4 MHz wide spectral bands ($\Delta v \approx 720$ km s^{-1}), dual polarization, 7.81 kHz ($\approx$1.7 km s^{-1}) channel width, and centered at the rest frequency of each line shifted by the recession velocity of the source given in Table 3. We use a single 8 MHz window with dual polarization and 7.81 kHz (1.65 km s^{-1}) channel width to cover the 1665 and 1667 MHz lines together. We center this window at 1666.3804 MHz shifted by the recession velocity of the source. The width of this window means that we always cover >500 km s^{-1} away from the galaxy systemic velocity. We expect to detect individual OH masers, while line stacking over large areas or absorption searches toward bright continuum sources will probe diffuse gas.
4. *Hydrogen radio recombination lines (RRLs).* We allocate the remaining correlator resources to place bands that cover hydrogen radio recombination lines (RRLs). We cover eight transitions: H175α, H171α, H170α, H166α, H158α, H156α, H154α, and H153α. These were down-selected from the available transitions favoring regions of the spectrum free of RFI and avoiding potentially noisy edges of subbands. These lines are known to be faint and expected to be challenging to detect given our exposure times and the distances to our sources (R. L. Brown et al. 1978; H. Beuther et al. 2016). The

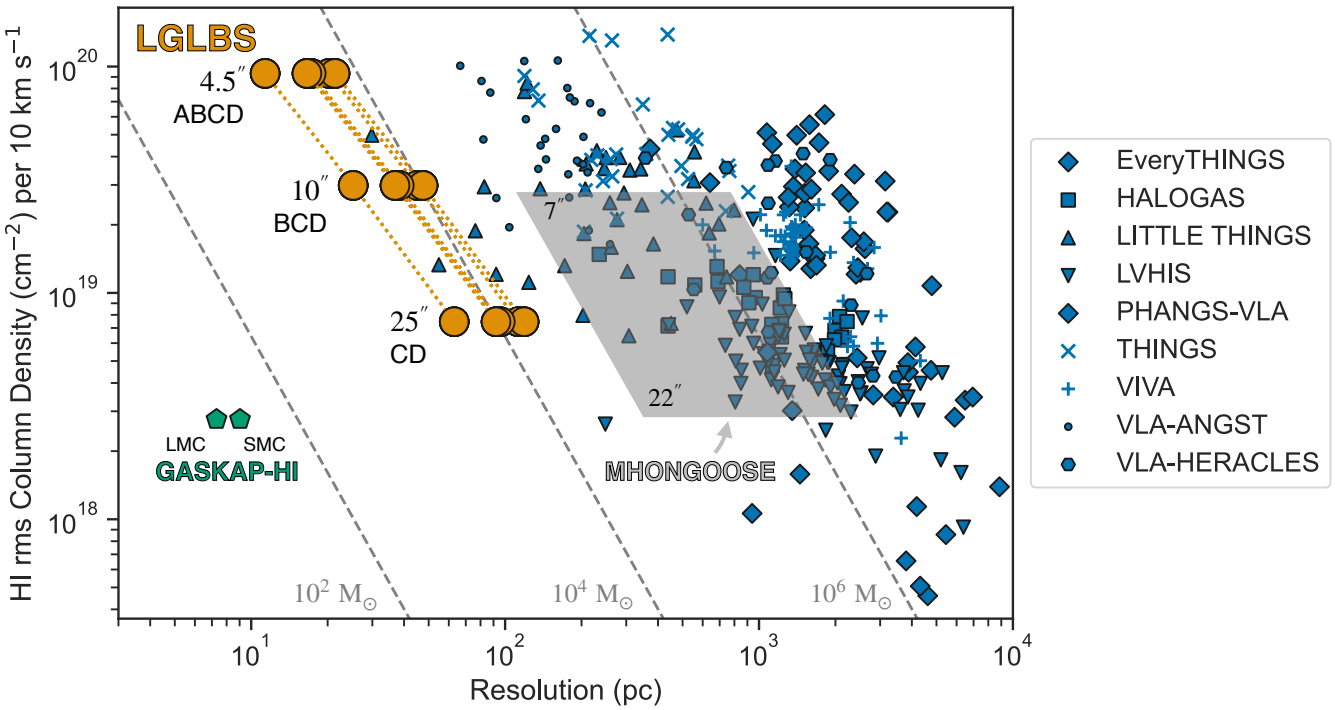

Figure 3. LGLBS H I column density sensitivity and physical resolution relative to comparable nearby galaxy and Local Group surveys. The LGLBS points show the range of sensitivity and resolution within the target velocity resolution, and the labels indicate the combination of VLA configurations combined to reach these targets. The dashed gray lines indicate constant 5σ H I mass sensitivity. LGLBS fills an important gap in the H I survey parameter space between the nearby galaxy population (e.g., EveryTHINGS, I. Chiang et al. 2025, in preparation; HALOGAS, G. Heald et al. 2011; LITTLE THINGS, D. A. Hunter et al. 2012; LVHIS, B. S. Koribalski et al. 2018; PHANGS-VLA, presented in J. Sun et al. 2022; THINGS, F. Walter et al. 2008; VIVA, A. Chung et al. 2009; VLA-ANGST, J. Ott et al. 2012; VLA-HERACLES, A. Schruba et al. 2011; MHONGOOSE, W. J. G. de Blok et al. 2024), and LMC and SMC (e.g., GASKAP-HI, N. M. Pingel et al. 2022), which are >10× nearer than any of the LGLBS targets. See also F. M. Maccagni & W. J. G. de Blok (2024).

data are obtained primarily as targets of opportunity and a potential archival resource for the community.

5. *Commensal REALFAST monitoring.* We worked with NRAO staff to ensure that our spectral setup was compatible with simultaneous REALFAST monitoring. REALFAST (C. J. Law et al. 2018) is a backend that processes VLA observations in parallel in real time to monitor for transients like fast radio bursts (FRBs). Thus, LGLBS also represents an extended transient search campaign toward our nearest neighbors, and R. Anna-Thomas et al. (2025) present two FRB detections toward M31 that are detected during LGLBS observations.

The archival data listed in Table 4 includes the polarization and 21 cm line coverage that was sufficiently similar to the LGLBS strategy that there was no utility to reobserving. In many cases, the continuum spectral channels were the same in the archival data but collected in eight 128 MHz SPWs. While this should make little difference in principle, it did introduce some practical issues using the CASA software package to combine these data with the new 20A-346 (CASA Team et al. 2022). Details of the OH and RRL coverage varied across the different archival projects. The 21 cm coverage can all be incorporated straightforwardly into our current observations.

4.2. Spatial Coverage

We created tailored mosaics that aim to cover the known 21 cm emission and ongoing high-mass star formation in each target. These are visualized in Figure 1.

1. *IC 10, IC 1613, and WLM.* The main star-forming regions and stellar disks of these three targets fit within a single VLA primary beam (Section 3), and we target one pointing in all four configurations (A, B, C, and D) to achieve maximum resolution and sensitivity in this region. All three also have evidence for more extended, though often low-column density H I emission (D. A. Hunter et al. 2012; J. Ott et al. 2012). To capture this, we observe all three targets with a seven-point hexagonal mosaic in the compact C and D configurations only. This extended coverage allows us to achieve high surface brightness sensitivity at coarser resolution over a large ($\gtrsim$10 kpc across) area.
2. *NGC 6822* has an inclined disk that is significantly extended compared to the VLA primary beam. We observe the galaxy using a three-point mosaic aligned with the H I major axis.
3. We observe *M33* using a 13-pointing mosaic that covers the high column density H I known from previous mapping (M. E. Putman et al. 2009; P. Gratier et al. 2010b). This mosaic is identical to that used in E. W. Koch et al. (2018b) to allow for easy combination of our new observations with these previous data (Table 4).
4. We observe *M31* using a 49-pointing mosaic. This covers the high column density H I known from previous mapping (R. Braun et al. 2009), but does not cover the outer disk of the galaxy (i.e., the extended low-column material beyond the optical radius of M31; R. Braun & D. A. Thilker 2004).

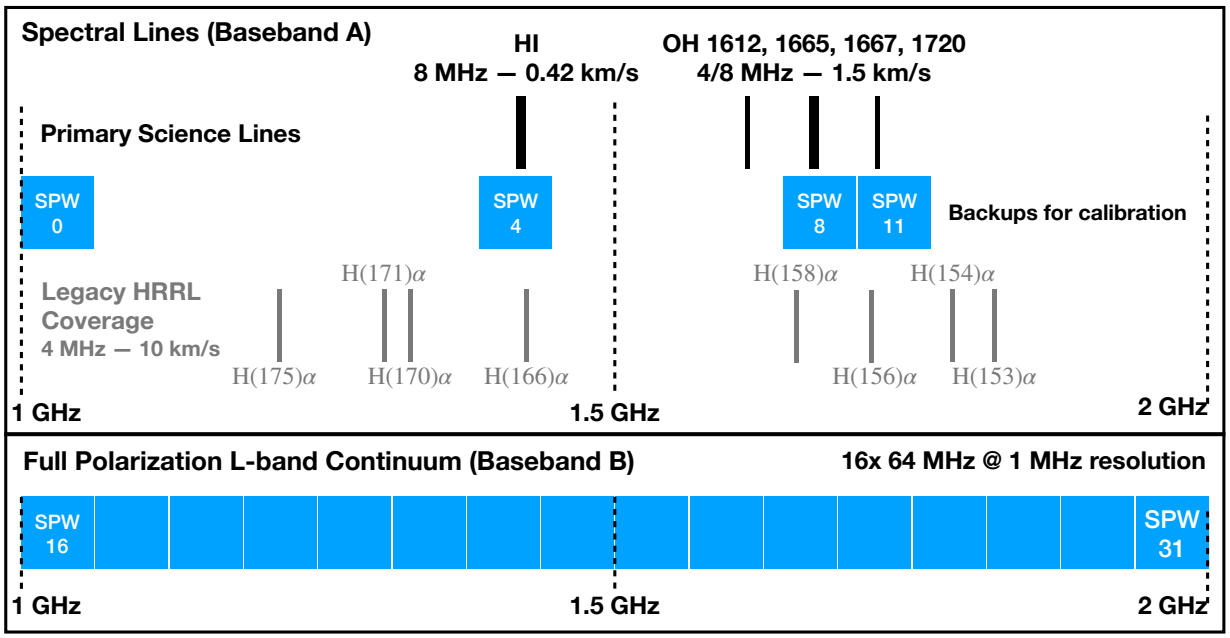

Figure 4. VLA correlator setup used for LGLBS (VLA Project ID 20A-346). The black, gray, and blue regions represent individual spectral windows (SPWs) used in the LGLBS setup. The primary LGLBS data products are the H I and 4 OH lines (black regions), and the Stokes I *L*-band continuum. Four continuum SPWs are also observed in Baseband A (labeled SPW 0, 4, 8 11 here) to allow for calibration checks between the basebands. The tuning also includes full polarization for the continuum windows shown in blue (with requisite polarization calibration observations taken) and eight hydrogen radio recombination lines (RRLs, black regions). Commensal data for FRB detections was collected with REALFAST for all LGLBS observations (C. J. Law et al. 2018). The Stokes I continuum, H I, and OH line coverage are similar in all archival observations (Table 4) but may not exactly match the tuning used for the primary LGLBS observations. The RRL and polarization coverage vary somewhat across the archival data but are all part of all LGLBS observations.

Table 3
Observational Properties of Targets

Property	IC 10	IC 1613	M31	M33	NGC 6822	WLM
PGC	1305	3844	2557	5818	63616	143
R.A. (hr)	0.3 hr	1.1 hr	0.7 hr	1.6 hr	19.7 hr	0.0 hr
Decl. (deg.)	+50°	+2.°3	+41.°3	+30.°6	−14.°8	−15.°5
v_{LSR} (km s^{-1})	−340	−238	−296	−180	−44	−122
C & D fields	7	7	49	13	3	7
A & B fields	1	1	49	13	3	1

Note. PGC catalog number used to cross-reference to HyperLeda (G. Paturel et al. 2003; D. Makarov et al. 2014). Velocities are the ones used in our correlator setup (Section 4.1) based on previous observations (Table 1) and the NASA Extragalactic Database. "C & D fields" and "A & B fields" refer to the number of fields in the mosaics for that target in those VLA configurations.

More than any other target, M31's large extent forces us to focus specifically on the disk of the galaxy.

We cover the observed area with a hexagonal grid of pointing centers, spaced by 1000″ (1048″for M31), which is approximately one-half of the FWHM primary beam size at 1.4 GHz. This coverage yields uniform rms noise across the mosaic, particularly in the lower half of the frequency band. The good overlap in coverage between adjacent pointings helps ensure even *uv* coverage so that losing a few scans to RFI has minimal impact. In principle, covering bright continuum sources in different parts of the VLA primary beam should improve our bright source reconstruction and deconvolution.

Table 4
Data Sets Included in LGLBS

Galaxy	Config.	Program ID	PI
All	A/B/C/D	20A-346	Leroy
co-PIs: Chomiuk, Dalcanton, Rosolowsky, Stanimirovic, Walter			
IC 1613	C	13A-213	Leroy
M31	D	14A-235	Leroy
M31	C	15A-175	Leroy
M31	B	15A-175	Leroy
M33	C	14B-088	Rosolowsky
M33	B	17B-162	Koch
M33	A	16B-232	Koch
M33	A	16B-242	Koch
NGC 6822	DnC	13A-213	Leroy
NGC 6822	DnC	14B-212	Schruba
NGC 6822	CnB	14B-212	Schruba
NGC 6822	CnB→B	14B-212	Schruba
WLM	DnC	13A-213	Leroy
IC 10	GBT	13A-430 & 13A-420	Ashley
IC 1613	GBT	16A-413	Pisano
M31	GBT	14A-367	Leroy
M33	GBT	09A-017[a]	Lockman
NGC 6822	GBT	13B-169	Johnson
WLM	GBT	16A-413	Pisano

Notes. 20A-346 represents the main survey. The other projects are archival projects that target the sample galaxies with similar spectral setups since the VLA upgrade.
[a] F. J. Lockman et al. (2012).

Our scan time, calibrator cycling time, and the length of individual integrations followed standard VLA recommendations for each configuration. Each mosaic was completely observed during every observation. Given typical observation durations of 3–5 hr, most mosaics were observed several times. However, each field in M31 could be observed only once per observing block. To ensure even *uv* coverage across M31, we scheduled observations with a variety of LST start times, and we also rotated the order in which we cycled through the mosaic pointings. In Section 6, we show derived H I products using the C and D configurations that demonstrate that the mosaics achieve a uniform sensitivity.

4.3. Target Depth and Balance between Configurations

As described in Section 2, we aim to pursue multiple science goals with a single set of observations. These science goals drive our sensitivity and resolution requirements to achieve four main observational goals:

1. Measure the line-integrated column density of the H I at <20 pc ($\approx 5''$) scales and reach rms column density sensitivity of $\approx 1 \times 10^{20}$ cm^{-2}. This is sufficient to measure the column density of individual clouds and identify H I shells and holes.
2. Measure high surface brightness, high-velocity resolution spectra of the 21 cm line at $\approx$40–60 pc ($\approx 10''$–$15''$) scales to allow for detailed spectral analysis. We target $\approx$4 K per 0.4 km s^{-1} channel.
3. Detect and resolve continuum emission from individual SNRs and H II regions, which have sizes of $\sim$10 pc ($\approx 2\farcs5$) and fluxes of $\gtrsim$10 μJy.
4. Recover the full 21 cm emission at all spatial scales accessible to the VLA, giving a complete view of the atomic gas in each galaxy.

Our observing strategy balances these goals and targets effective per-point integration times by configuration of 11 hr in A, 11 hr in B, 11 hr in C, and 5.5 hr in D. We account for the oversampling of the mosaics when working out the target time per field. The high-resolution goals, especially the continuum, push us to weight the high-resolution VLA A configuration heavily. Those emphasizing surface brightness sensitivity, especially in narrow velocity channels, benefit most from the intermediate B and C configurations. Sensitivity to extended emission requires the D configuration.

Our adopted balance of time between different configurations differs somewhat from the "rule of thumb" that prescribes a 3:1 ratio between successive configurations and was used by previous H I surveys (F. Walter et al. 2008; D. A. Hunter et al. 2012; J. Ott et al. 2012). This reflects that our A configuration science drivers are heavily weighted toward continuum, which has less stringent surface brightness sensitivity requirements than 21 cm imaging and benefits from larger bandwidth. It also reflects a practical acknowledgment that fully leveraging the high spectral resolution (which divides the line signal into many dozens of individual channels) requires emphasizing the intermediate configurations. We validated that this balance of configurations yields reasonable point-spread function (PSFs) using simulations, and our resulting imaging closely matches the simulated expectations.

4.4. Short and Zero-spacing Data

Our targets all show significant extent compared to the largest angular scales to which the VLA C and D configurations are sensitive. This largest recovered scale is $20\farcm5$ for the 21 cm H I line, and ranges from $29\farcm4$–$14\farcm7$ from 1–2 GHz across the *L*-band continuum. For the 21 cm line, GBT observations exist for all of our targets at an appropriate depth to serve as short- and zero-spacing observations. The individual projects are listed in Table 4, and thanks to the upgraded GBT VEGAS backend, most have a velocity resolution appropriate for combination with our VLA observations. We describe the reprocessing and imaging of the GBT observations for NGC 6822, IC 10, IC 1613, and WLM in Appendix A. In Appendix B, we describe the short-spacing correction by feathering and relative flux comparison tests for the GBT and VLA 21 cm H I observations.

In principle, the continuum observations also require short- and zero-spacing corrections. This problem is more acute than for the spectral lines since the Doppler shift across the galaxies means the line emission only appears in a spatially confined region, while continuum emission spans the entire galaxy. Unfortunately, stable, high-quality *L*-band single-dish continuum mapping is challenging (e.g., R. Beck et al. 1998) and has been almost exclusively restricted to narrower frequency ranges to avoid instability from RFI. Identifying or obtaining a suitable set of zero-spacing maps that span the full 1–2 GHz range remains a future goal. For now, our continuum science emphasizes compact scales and individual objects. Individual H II regions or SNRs have sizes far smaller than the largest angular scales recovered by the C and D configuration and should be robustly imaged by using our VLA data alone.

5. Data Reduction and Quality Assurance

Although the VLA calibration pipeline works well, the presence of substantial RFI in the *L* band and occasional issues with antenna performance mean that most tracks require additional flagging and quality assurance (QA) checks before imaging. To deal with the substantial data volume of LGLBS, the need for rapid review of observations, and the distributed nature of our team, we developed a custom QA system. This system is publicly available and composed of the `ReductionPipeline`[34] and `QAPlotter`[35] packages. These packages can easily be adapted to process any non-LGLBS VLA *L*-band data taken using the WIDAR correlator.

Our system expands upon the quality assurance and flagging capabilities in the current VLA pipeline, adding additional interactive capabilities that can be used to identify poor-visibility data. Our system stores all data in a single compute facility, and team members perform QA review remotely using a web browser. Thus, a team member never needs direct access to the visibility data. Users specify flagging commands to eliminate bad data from subsequent pipeline calibration. The system then implements those manual flags, reruns the calibration, then serves up new interactive plots, allowing users to iterate until all bad data are removed from the calibration and the resulting calibration appears robust.

[34] https://github.com/LocalGroup-VLALegacy/ReductionPipeline
[35] https://github.com/LocalGroup-VLALegacy/QAPlotter

5.1. Data Reduction

Our procedures build on the VLA pipeline.[36] As observations were taken over multiple years, we updated to use new pipeline versions as they were released. Our calibration used CASA VLA Pipeline versions ranging from 6.1.2–7 to 6.5.4–9.

As recommended in the NRAO documentation, we split the data into separate continuum and spectral line measurement sets prior to running the reduction pipeline. This allows us to apply Hanning smoothing to the continuum data, which minimizes Gibbs ringing due to strong RFI. We do not smooth the spectral line data, which are instead processed at their native resolution. Narrow H I features on scales similar to the $\sim$0.4 km s^{-1} channel width are important to our science goals (Section 2), and these would be degraded by smoothing. Fortunately, RFI is typically weaker in our H I data because our source redshifts fall within the protected part of the spectrum.

Most of the pipeline steps calibrate per SPW, so splitting the data has minimal effect on the calibration solutions. The exception is flux bootstrapping between calibrators. For each calibrator, the VLA pipeline calculates the average flux in each SPW and then fits these together to constrain the spectral index and flux. Then, the pipeline bootstraps from the flux calibration standard to infer the flux of the secondary calibrators (i.e., those used to measure gain, polarization angle, and leakage) based on the results of these fits. Because the spectral coverage varies between the continuum and spectral line parts, the bootstrapped fits could, in principle, be different. However, based on reviewing a subset of tracks, we find differences of $<5\%$ between the boostrapped fluxes for the same calibrator in the line and continuum parts. This is within the expected absolute flux uncertainty for the VLA at the *L* band.[37]

5.1.1. Continuum Data Reduction

The VLA pipeline is optimized for continuum calibration, and we follow the standard pipeline recipe for continuum data. For the *L* band, the heuristics in the pipeline work well for flagging strong RFI and determining where calibration solutions have failed. However, we still find it useful to add two flagging routines to the standard pipeline. First, we flag the one or two continuum channels closest to the target's H I emission in order to remove potential bias due to line contamination in the continuum images. We found that when the VLA is in the compact C and D configurations, the H I emission was strongly detected in the continuum channels for many fields in M31 and M33. Second, we moderately increase the time interval in the `quack` RFI flagging routine to flag the first three integrations of each scan. This flagged many cases where a subset of antennas began observations before others, which appear as integrations with sparse *uv* coverage at the start of the science scans after applying the observatory-generated flags.

5.1.2. Spectral Line Data Reduction

We make several modifications to the standard VLA pipeline to optimize it for the LGLBS spectral line setup. First, following the VLA pipeline guide, we automatically specify line frequency ranges where we expect astronomical signal. This helps avoid the case where the automated RFI flagging routines confuse spectral line features with RFI and flag them by accident. The specific protected spectral ranges are defined per galaxy based on the velocity ranges in the kinematic LSR (LSRK) frame known to exhibit H I emission. We also include a protected range near 0 km s^{-1} in all of our target fields to avoid flagging foreground Galactic H I emission and absorption.

For the spectral line data on the science targets, we also disable some automated RFI flagging routines altogether. We found that the built-in heuristics, which have been primarily tested on continuum SPWs, flagged very few data in comparison to the amount of time needed to run these routines. We note that this might not be an optimal choice for other line observations. Our Local Group targets have small systemic velocities, so the source emission still falls within protected radio-quiet frequency ranges. These small Doppler shifts result in minimal RFI in the H I and OH line (1665/1667 MHz) windows.

We also add capabilities to handle the Galactic H I foreground toward the calibrators, where the intervening gas creates absorption features in the calibrators' continuum spectra. For each calibrator, we define and flag a velocity range based on H I absorption spectra where available (e.g., following 21-SPONGE; C. E. Murray et al. 2015). When an H I absorption spectrum is not available, we examine the H I SPW from the first observations and define a velocity range based on the observed H I absorption. Avoiding Galactic H I absorption is crucial for bandpass calibration and further directly impacts H I measurements in our science targets, as M31 and NGC 6822 overlap in velocity with Galactic H I. To recover this velocity region for the bandpass solution, we interpolate across the flagged gap using a Savitzky–Golay filter with handling for complex values. This approach is stable because, for the 8 MHz bandwidth that we use for the H I, the bandpass response of the VLA varies smoothly on scales much larger than the Galactic H I velocity width. This procedure is not needed for the OH lines, which do not show obvious Galactic absorption features at a level that affects our calibration procedures.

5.2. Quality Assurance

We found that despite the good performance of the pipeline, residual RFI was often present, and other technical issues also persisted after the automated calibration. In practice, we found that the best practical way to address this was manual inspection of the calibrated data set produced for each 3–5 long scheduling block. During this manual inspection, the reviewer identifies egregious or systematic issues affecting the calibrated data or the calibration and then creates manual flagging commands to remove these issues. After inspection, subsequent pipeline runs use these manual flagging commands. Team members then inspect the newly calibrated data using these additional flags, repeating the process until we have final, well-calibrated visibility data.

[36] https://science.nrao.edu/facilities/vla/data-processing/pipeline
[37] https://science.nrao.edu/facilities/vla/docs/manuals/oss/performance/fdscale

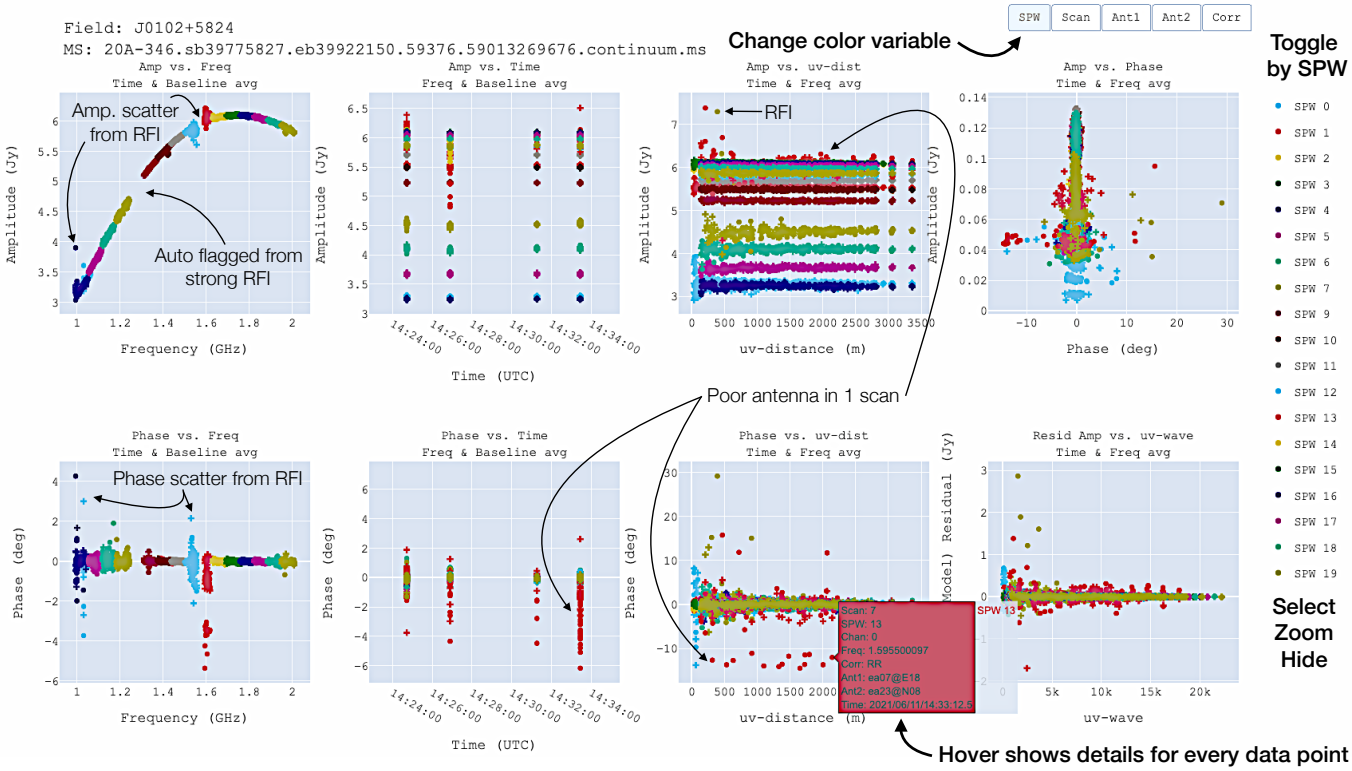

Figure 5. Example of an interactive plot used to quality assure LGLBS visibility data. Calibrated visibilities for the gain calibrator J0102+5824 (used for NGC 6822 observations), with plots showing average amplitude and phase as a function of time, frequency, antenna, and *uv* distance. This plot shows the initial calibrated visibilities from the pipeline without additional manual flagging applied. We indicate several cases of additional RFI that were not automatically flagged, and an example of a set of poor amplitude/phase baselines arising from a single antenna in one scan. In bold text, we highlight features of the interactive plots that enable rapid identification of visibility errors, including the interactive key where data from individual SPWs can be toggled to select, hide, or zoom to a subset of the data.

5.2.1. Interactive QA Plots

Our distributed QA system uses a web browser to provide a visualization interface. This includes bespoke interactive visibility and calibration plots and an automated review and restart procedure built around a series of Google Sheets linked to CASA scripts. Specifically, we load the data into the CASA task `plotms` and produce a series of projections of the visibility data that are exported as text files. These summary files are automatically created as the last step in each pipeline run.[38] After the pipeline run, a separate package (`QAPlotter`[39]) imports these data and collates the quick-look images used for QA into interactive figures using `astropy.table` and `plot.ly`. The HTML figures created by `plot.ly` have interactivity including panning and zooming. Finally, the `QAPlotter` software exports the HTML plots to a webserver that is available via a browser to any team member and embeds them in an HTML framework that makes it easy to navigate between the different QA plots.

Our goal in manual QA is for a team member to identify and flag calibration or data issues that had been missed by existing algorithmic or heuristic-based measures. To enable this, we create three types of interactive plots:

1. Summary plots showing the final calibration tables, including the amplitude and phase bandpass tables, and the phase and amplitude gains as a function of time.
2. Visibility summary plots per calibrator and science field, averaging over combinations of frequency, time, and *uv* distance to minimize data volume. For science fields, we create panels showing amplitude versus time, frequency, and *uv* distance. For calibrators, we also include panels showing phase as a function of time and frequency, as well as amplitude and phase versus antenna number. The latter allows us to identify systematic issues per antenna. Figure 5 shows an example visibility summary plot for the gain calibrator J0102+5824.
3. Quick-look imaging of each SPW for each field with no deconvolution (also known as the "dirty image"). This allows us to quickly assess the imaging quality. It also allows us to (roughly) assess the achieved noise level and compare it to the theoretically expected noise. We analyze these quick-look images to create interactive scatter plots of the noise per SPW and per field. Anomalously high noise levels proved useful to quickly identify poorly calibrated visibilities. Figure 6 shows an example of quick-look continuum images for a single field in M33.

Each of these interactive plots retains sufficient metadata to identify the frequency, time, antenna, baseline, and polarization associated with outlier data or other issues. These metadata also enable changing the color of points in the visibility summary plots to expose different data axes (e.g., users could quickly switch between coloring by polarization or

[38] We built standard export functions for each interactive plot type that can be used with most VLA data sets that have been reduced with recent versions of the VLA reduction pipeline. These routines assume naming conventions adopted for the VLA pipelines associated with CASA versions >6.1.

[39] Similar to the CASA export step, much of the `QAPlotter` implementation can be adapted for use with other interferometric data from different telescopes.

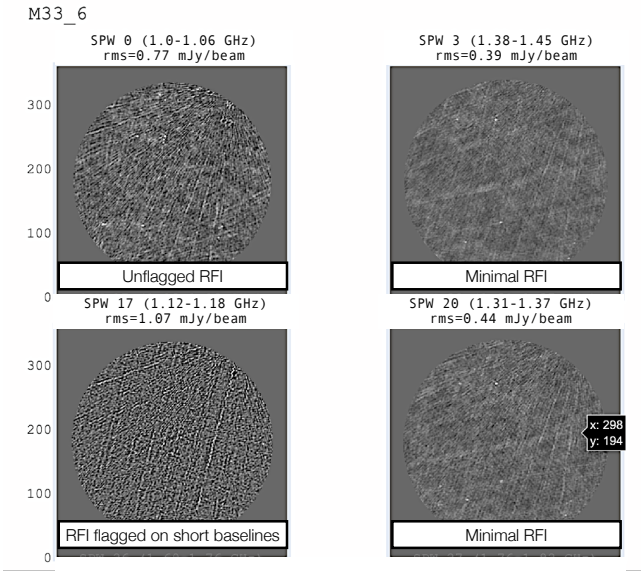

Figure 6. A subset of quick-look imaging for a single M33 field shows examples used to quality assure LGLBS visibility data, which the LGLBS pipeline generates for every science field. We show four examples generated from single 64 MHz continuum SPWs with no deconvolution applied. The left column shows examples of poor data quality, due to either remaining RFI that requires flagging (top) or where strong RFI has been automatically flagged by the VLA pipeline (bottom). The right column are examples of SPWs with minimal strong RFI remaining, where the artifacts are consistent with the VLA's point-spread function (PSF) shape.

SPW in an amplitude versus time plot). Finally, we also include the ability to focus on individual chunks of the data through interactive legends; for example, selecting only a subset of SPWs or fields to be shown in a visibility summary plot is possible.

5.2.2. Common Issues Identified in QA Process

Using these tools, we have quality assured more than 430 individual tracks (∼1800 hr; including archival VLA observations) as of this writing, distributing the work among 21 team members[40] and iterating each track until it is properly calibrated. Another 60 tracks, all targeting M31 in A configuration, are currently undergoing iteration in QA.

Since QA effort is distributed over a broad group, we began the QA process with a smaller team with significant previous experience with interferometry data reduction to produce a "best-practices" QA guide to help ensure that our review process was uniform among reviewers. Based on the aggregate statistics shown below in Section 5.2.3, we do not find significant differences in the flagging statistics after QA between individual reviewers.

While the vast majority of systematic issues are correctly caught and handled with the VLA pipeline heuristics, we highlight some common issues in the LGLBS data identified during this experience. We expect that continued development of the pipeline will further reduce the need for manual flagging.

At the *L* band, particularly for continuum data, the most common issue flagged is transient RFI at persistent frequencies. In practice, our reviewers mostly manually flagged RFI that appeared as >0.1 Jy in amplitude versus frequency plots created after averaging over the duration of a scan (∼3–5 minutes) and all antennas. We verified that this flagging does moderately lower the estimated noise in the resulting quick-look images.

The QA process also frequently identified poorly performing antennas that show anomalously low amplitudes or individual outlying baselines. Poorly performing antennas were frequently evident in the bandpass table, where amplitudes >3× lower than the median of the remaining antennas lead to visible increase in the scatter in subsequent gain calibration solutions. Many of these per-antenna or per-baseline issues correspond to issues noted by operators in the observing logs but not flagged automatically by the pipeline. We also identified some rarer issues, including a handful of cases where single antennas have anomalously low amplitudes (>100× lower but nonzero), but only in individual scans.

Finally, we note that for the OH 1612 MHz line, significant velocity ranges are often lost due to persistent, strong RFI near 1615 MHz. In our survey, this most significantly affects M31, where the blueshifted southern half of the galaxy with recession velocity from $v_{\rm LSRK} \sim -300$ to -500 km s^{-1} falls in this frequency range. In these cases, we remove the most egregious RFI frequency ranges and attempt to recover as much of the redshifted half of M31 as the data allow.

The manual flagging produced through our QA procedure offers a valuable set of labels for training machine learning approaches to identify common issues in interferometric data. The data have uniform spectral coverage, common processing, and repeated visits to every field over ∼1 to 10 yr timescales (including the archival projects; see Table 4), making them an ideal reference set. The next generation of radio interferometers (e.g., SKA or ngVLA; R. Braun et al. 2015; E. J. Murphy et al. 2018) will require extending these manual or automated procedures to cope with the expected data rates.

5.2.3. Flagging Statistics after QA

Here we quantify the overall flagging fractions based on a representative sample of 337 LGLBS tracks (all with project code 20A-346) reflecting the qualitative description of common QA issues.

Figures 7 and 8 summarize the flagging percentages across the continuum and spectral line SPWs for the LGLBS targets using 337 LGLBS tracks that provide representative statistics for the whole survey. As indicated on both figures, ∼15% of the flags result from systematic flagging (channel edges, first three integrations, etc). We calculate the flagging percentages in each track using the statistics saved in the VLA pipeline weblog, which we average across antennas and fields in each track to measure the total flagged percentage in each SPW. Figure 7 shows the median flagging percentage versus frequency, where the error bars indicate the 15th–85th percentiles across the 337 tracks.

Consistent with RFI spectra at the VLA site, Figure 7 shows that we typically fully flag continuum SPWs from 1.1–1.3 GHz and 1.5–1.6 GHz, with the lowest data losses between 1.3–1.45 and 1.6–1.9 GHz. The spectral line SPWs have similar or

[40] QA participants include: Haylee Archer, Alberto Bolatto, Katie Bowen, Michael Busch, Hongxing Chen, Serena Cronin, Harrisen Corbould, Jeremy Darling, Thomas Do, Jennifer Donovan Meyer, Cosima Eibensteiner, Marcus Graham, Deidre Hunter, Eric Koch, Timea Kovacs, Lauren Laufman, Adam Leroy, Jarod McCoy, Amit Kumar Mittal, Hailey Moore, Nickolas Pingel, Erik Rosolowsky, Daniel Rybarczyk, Sumit Sarbadhicary, Amy Sardone, Snezana Stanimirovic, Ioana Stelea, Jiayi Sun, Elizabeth Tarantino, and Vicente Villanueva.

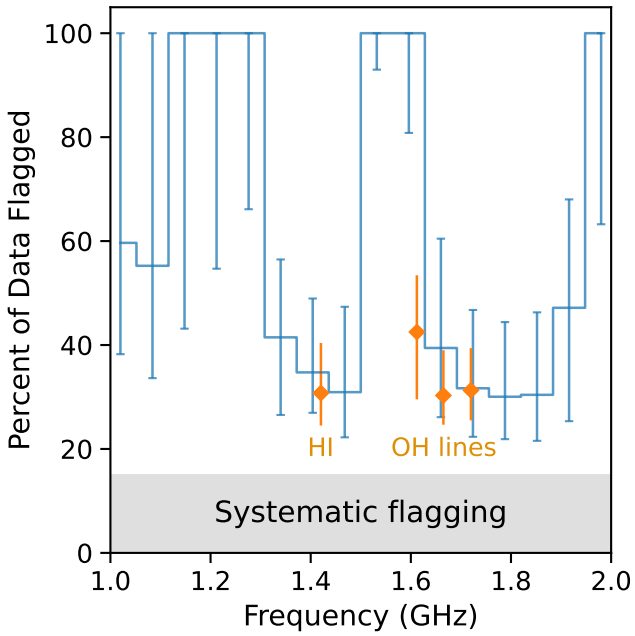

Figure 7. Median percent of flagged data per SPW, where the error bars reflect the 15th–85th percentile range of 337 LGLBS tracks. The continuous blue lines indicate flagging percentages for the continuum SPWs, and the orange diamonds are the line SPWs for H I and the four OH lines (the OH1665/1667 are recorded together in the same SPW). The current LGLBS processing does not include the hydrogen RRLs included in the spectral setup.

moderately lower flagging fractions relative to the continuum SPWs, consistent with the location of these lines in protected bands near the rest frame (for H I, OH1665, OH1667) or in minimal-RFI contaminated ranges (OH1720). As noted above, the OH1612 rest frequency falls near to strong and persistent RFI, though only the redshifted edge of OH1612 for M31 significantly overlaps with this strong RFI range.

Figure 8 shows the cumulative distribution functions (CDFs) of data flagging percentages for the continuum and line SPWs. In general, these highlight the trends visualized in Figure 7 but also show the full distributions of SPW flags in the sample of 337 tracks. For the continuum SPWs, the CDFs show the high loss fraction for SPWs with strong and persistent RFI (particularly near 1.5 GHz). For the line SPWs, we find comparable statistics for H I and OH1665/67, consistent with much of our bands falling within the protected frequency ranges. OH1720 has similar flagging statistics, reflecting the minimal RFI at these frequencies, but OH1612 has a consistently higher flagging fraction because of its proximity to strong RFI sources. For each of the lines, we note that the aggregate flagging statistics reflect the whole SPW bandwidth, while our target velocity ranges typically fill 20%–50% of the SPW. Hence, the line flagging statistics present a pessimistic view of the spectral line sensitivity as RFI preferentially occurs closer to the edge of the protected bands (see Section 5.4).

5.3. Data Products

In later LGLBS data releases, we will deliver the final calibration tables and flag versions of each track to the NRAO archive, allowing other users to regenerate calibrated visibility data. A final description of these products will accompany each LGLBS data release.

For our own processing, after a track passes QA, we split the calibrated visibilities of the science targets from the original measurement sets to minimize the data volume. The calibrated science data are then transferred to persistent storage to be accessed for subsequent imaging using separate approaches for spectral lines (N. Pingel et al. 2025, in preparation) and continuum (S. Sarbadhicary et al. 2025, in preparation).

5.4. H I Resolution and Sensitivity Achieved in LGLBS

We test whether the LGLBS observations reach the project's proposed resolution and sensitivity goals using observations of the central field of IC 10. This field was observed to the nominal depth using all four VLA configurations. After calibration, we pre-process the data, including continuum subtraction, following the steps outlined in Section 6 using the PHANGS–ALMA imaging pipeline (A. K. Leroy et al. 2021). Specifically, we subtract the continuum component from the visibilities using CASA's `uvcontsub` task with a linear fit. We fit the continuum component excluding the target's velocity range to avoid all line emission from the fit. We also exclude the outer 10% of the bandwidth (including the edge channels flagged by the pipeline) as we found that the continuum fits were biased to moderately lower amplitudes when including this portion of the bandwidth; this led to minor variation only for the brightest (>50 mJy) sources. After continuum subtraction, we image a single 1.2 km s^{-1} channel without detected H I using different combinations of VLA array configurations and varying the weighting scheme used to grid the visibilities from uniform to robust (Briggs parameter from $r = -2$ to 2) to natural. Figure 9 shows the rms intensity in the channel, the equivalent column density sensitivity over a 10 km s^{-1} window, and the H I mass per beam for each imaging exercise. We show these for each array configuration and combination of array configurations and as a function of the beam semimajor axis.

During this imaging process, we noticed residual continuum emission from the brightest sources (>100 mJy) within the frequency range that we excluded from automated RFI flagging with the VLA pipeline. In these cases, all emission (line and continuum) had a step-like function constant amplitude increase within the "protected" frequency range that RFI flagging was not applied on. We suspect that this amplitude difference results from low-level RFI that contributed to the continuum component relative to the spectral line and is only statistically significant toward the brightest continuum sources. Indeed, comparing against previous imaging from E. W. Koch et al. (2018b, 2021) shows there is no significant offset in the total H I emission over the whole galaxies. To correct for this effect, we fit linear functions to the continuum-only channels, using aggressive sigma-clipping to exclude all H I emission, within the frequency/velocity range where RFI flagging was not applied and subtracted this model from the velocity range (including H I emission) in these spectra. This process removes all significant residual continuum emission, which we found was only present for a handful of bright sources in M31 and M33.

The figure shows that our data reach our target resolution and sensitivity, which are indicated by the labeled shaded gray lines in the center panel. This visualization also shows the benefits of combining the intermediate VLA configurations with the extended (A) and compact (D) baseline coverage. Our adopted 1:1:1:0.5 time-per-configuration ratio for A:B:C:D,

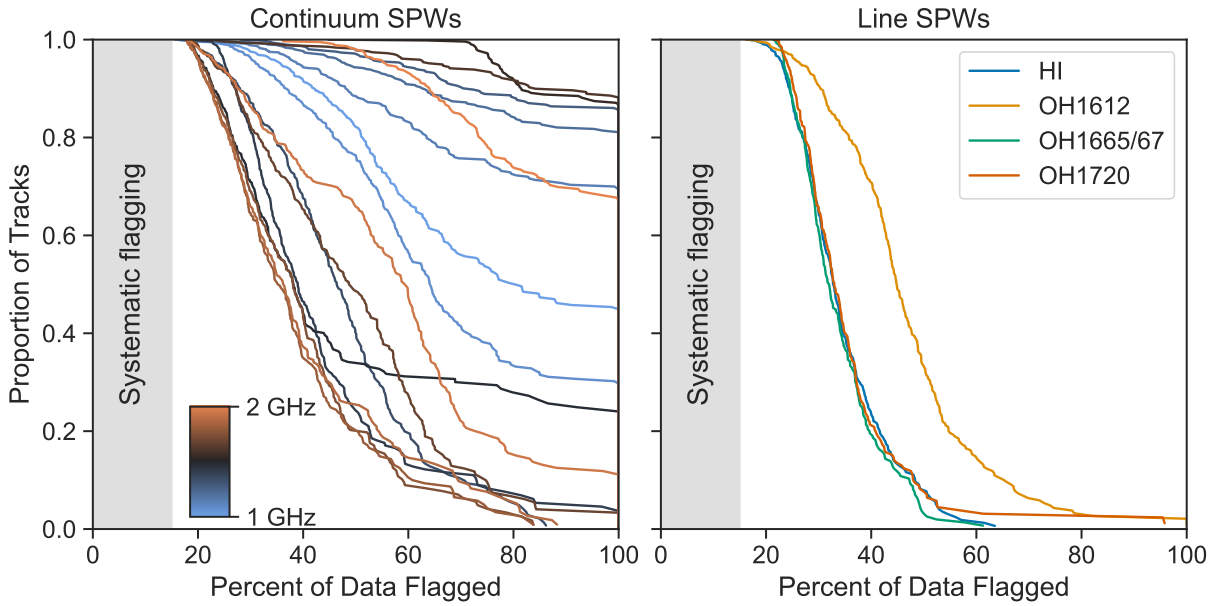

Figure 8. Cumulative distribution functions (CDFs) of the percent of flagged data split by SPW over 337 LGLBS tracks. Left panel: flagging percentage CDFs for the sixteen 64 MHz continuum SPWs covering 1–2 GHz. Right panel: flagging percentage CDFs for the H I and four OH line SPWs.

combined with varying the weighting scheme yields a nearly continuous range of beam sizes with the target column density sensitivity from 2″–60″.

6. LGLBS's 120 pc Resolution View of 21 cm H I Emission

Figures 10, 11, 12, 13, 14, and 15 show the wide-field, ∼20″ resolution H I images of the LGLBS targets. As described in Section 4, we observed seven-pointing hexagonal mosaics in the C and D configurations for IC 10, IC 1613, and WLM. In NGC 6822, we observed a common set of three pointings in a linear mosaic in all four configurations. We targeted M33 using a 13-point mosaic that spans the star-forming disk, and we cover the majority of M31 with a 49-point hexagonal mosaic. These images show the C and D configuration data imaged with robust 0.5 weighting (as defined in CASA's `tclean`) and short-spacing corrected using the GBT single-dish data. Imaging using all four configurations will appear in N. Pingel et al. (2025, in preparation).

We image the 21 cm emission for each target using an adapted version of the PHANGS–ALMA imaging pipeline (A. K. Leroy et al. 2021). We construct versions of the cubes with channel widths of 0.8, 2.1, and 4.1 km s^{-1}. We use a wide range of scales, 0, 10″, 30″, 100″ and 300″, for the multiscale deconvolution. Including these large scales is critical to achieve good results for the 21 cm emission, in which much of the flux often lies in an extended, relatively smooth distribution. After the multiscale clean, we identify regions of significant emission and apply a single-scale clean down to a depth of 1σ–2σ, considering the results to be converged when successive calls to `tclean` with a large number of components result in little change in the total flux of the clean model. The procedure for the PHANGS–ALMA imaging process resembles the one used to image VLA 21 cm emission from M33 H I in E. W. Koch et al. (2018b), and so has already been shown to yield excellent results for a similar Local Group H I data set.

We feather the deconvolved VLA H I cubes with the GBT H I cubes (see Appendix A) using `uvcombine` and the relative flux scaling factors measured in Appendix B. For NGC 6822, Appendix C describes our process to create an NGC 6822–only GBT H I cube with local pixel-wise infilling (A. K. Saydjari & D. P. Finkbeiner 2022) and manual masking of Galactic H I in the VLA cube.

Table 5 provides the 5σ H I column density and mass per beam in all targets after convolving to a common physical scale of 120 pc. We estimate the noise levels for each target from the rms scatter in 10 signal-free channels, considering only the central 120′ of each mosaic, where the maps all have uniform sensitivity. Our H I maps trace column densities of 1.4–4.1 × 10^{19} cm^{-2}, equivalent to H I surface densities of 0.1–0.3 $M_\odot$ pc^{-2}, which extends far into the atomic-dominated regime as predicted by photodissociation region models (e.g., M. R. Krumholz et al. 2011) and well beyond the traditionally defined edge of the H I disk at $\Sigma_{\rm HI} = 1\ M_\odot$ pc^{-2} (e.g., J. Wang et al. 2016). Expressed as point-mass sensitivity, these maps are sensitive to clouds of mass 1.8–4.1 × $10^3\ M_\odot$ per beam and thus are able to detect even individual low-mass clouds, including high-velocity clouds (e.g., M. E. Putman et al. 2012) or the atomic gas associated with molecular clouds.

We produce signal masks[41] and moment maps, again following the PHANGS–ALMA pipeline procedure A. K. Leroy et al. (2021). In Figures 10, 11, 12, 13, 14, and 15, we show the resulting integrated intensity, peak brightness temperature, centroid velocity, and effective width maps.[42] These are the deepest ∼100 pc wide-field views of H I in these Local Group galaxies, and the figures show the excellent imaging quality of the VLA that we achieve with the LGLBS observing strategy.

We measure the total H I masses in our fields of view from the integrated intensity maps produced using the "broad" signal mask (see A. K. Leroy et al. 2021), which emphasizes flux completeness at the expense of moderately increasing the

[41] We list further details and relevant parameters used for the masking with the data release.

[42] Effective width is defined as $\sigma = I_{\rm HI}/\sqrt{2\pi}\ T_{\rm peak}$, where $I_{\rm HI}$ is integrated intensity, and $T_{\rm peak}$ is the peak brightness temperature (e.g., J. Sun et al. 2018).

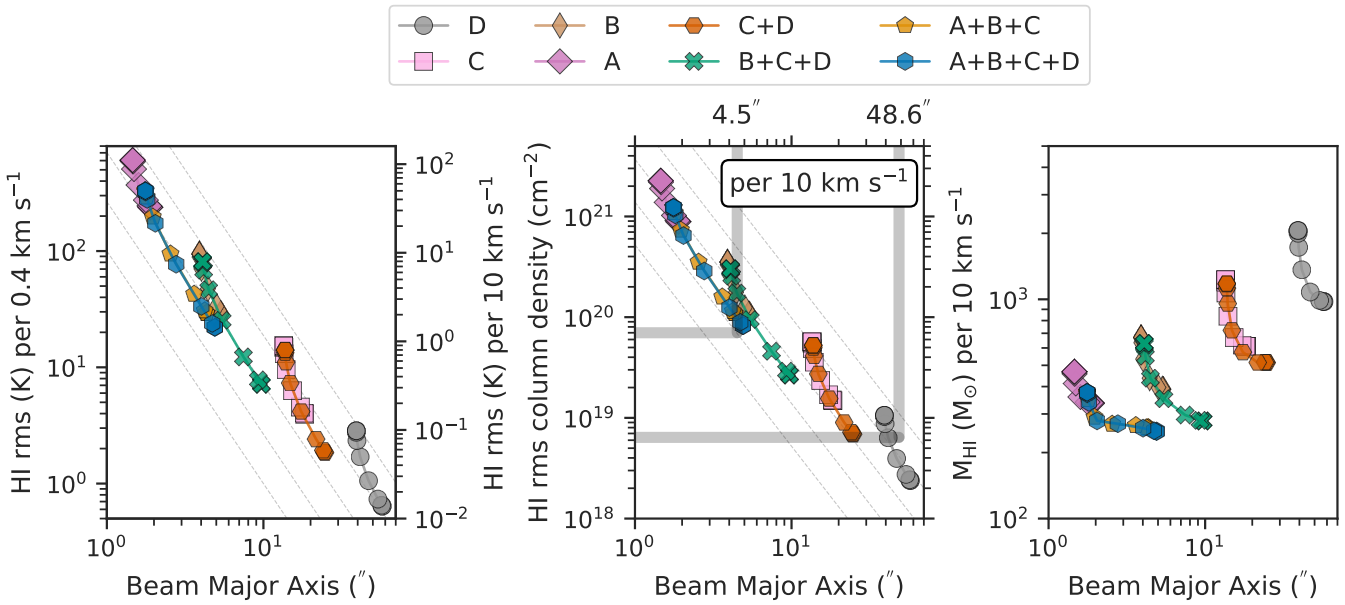

Figure 9. Measured H I intensity (left panel), column density (center panel), and mass per beam sensitivity (right panel) using observations of our central IC 10 pointing. Each color corresponds to a different array configuration or combination of array configurations (see the legend). The points connected by lines for each color show the effect of varying the weighting scheme used to grid the data (from uniform, through robust with Briggs parameter −2 to 2, to natural weighting). The left panel shows the rms noise for 21 cm intensity in an individual $\Delta v = 0.4$ km s^{-1} channel. The middle panel shows the implied column density sensitivity given the measured noise and integrating over a 10 km s^{-1} width. The right panel shows the mass sensitivity per beam, also assuming a 10 km s^{-1} velocity integration window. The gray dashed lines in the left and center panels indicate the expectation from statistical averaging of a constant noise map. Deviations from this reflect the loss of sensitivity when fewer baselines are included at coarse resolution. The solid gray lines in the center panel note the target resolution and sensitivity goals for the survey at the finest (4.″5 at 7×10^{19} cm^{-2}) and coarsest (48.″6 at 6×10^{18} cm^{-2}) scales. We reach within ∼20% of the target sensitivity at 4.″5 and moderately exceed the target sensitivity at 48.″6.

noise level. We adopt the sum of the integrated intensity error maps to estimate the uncertainty, corrected for the number of independent beam areas. Table 5 reports the measured atomic gas masses for these targets, assuming optically thin H I emission (equivalent to a conversion factor of 0.0146 $M_\odot$ pc^{-2}/K km s^{-1} when converting from H I integrated intensity). Assuming that the absolute flux calibration has an inherent 5% uncertainty, we also report an estimated systematic uncertainty that is dominated by the ≈5% flux calibration uncertainty. Table 5 provides measurements for the H I mass of each galaxy within our field. Based on the spatial extent of our targets, we expect that the area of our mosaic leads to a modest underestimate of the total H I mass in M31, M33, and NGC 6822.

In M31, within our field of view, we measured a total H I mass of 5.7×10^9 $M_\odot$. This is in good agreement with the approximate 5×10^9 $M_\odot$ quoted by R. Braun & D. A. Thilker (2004) and J. Yin et al. (2009) and close to the total H I mass of 5.3×10^9 $M_\odot$ estimated by T. M. Dame et al. (1993), but larger by 30% to the 4.1×10^9 $M_\odot$ measured by L. Chemin et al. (2009). Our M31 map covers most of the disk but clearly misses some of the extended disk (see R. Braun & D. A. Thilker 2004; R. Braun et al. 2009).

For M33, we find an H I mass of 2.0×10^9 $M_\odot$, within 3% of the H I mass from M. E. Putman et al. (2009). While some H I recovered in the M. E. Putman et al. (2009) M33 map is excluded by our more limited field of view, we note that M. E. Putman et al. (2009) found a total mass of 3.6×10^8 $M_\odot$ beyond the bright H I disk (defined as below an H I column density of 3.2×10^{20} cm^{-2}), of which we recover ≈30% in the LGLBS map. Thus, the discrepancy for the missing H I component falls within the total statistical and systematic uncertainty for our H I mass measurement. Relative to E. W. Koch et al. (2018b), who calculated an H I mass of 1.4×10^9 $M_\odot$ using a portion of the C configuration VLA data and the same GBT data we use here, the H I mass we find is 30% larger. Similar to the larger flux correction factor we find (see Appendix B), this difference reflects the improved VLA sensitivity and vastly improved short baseline coverage from including VLA D configuration data.

For NGC 6822, our H I mass measurement of $(1.9 \pm 0.1) \times 10^8$ $M_\odot$ is 20% larger than the mass from W. J. G. de Blok & F. Walter (2006) and 19% larger than B. Namumba et al. (2017). We expect our larger value is primarily due to differences in separating the Galactic H I foreground, which we have carefully modeled and removed here (see Appendix C). This appears to represent a larger effect than the modest fraction of the extended disk missed by our mosaic.

The other three dwarf galaxies all lie completely within our fields of view with little concern regarding Milky Way contamination. For IC 10, we find an H I mass of $(7.5 \pm 0.1) \times 10^7$ $M_\odot$ that agrees within the uncertainty with the value from LITTLE THINGS (D. A. Hunter et al. 2012) but is 14% smaller than measurements from the GBT (D. L. Nidever et al. 2013) and DRAO Synthesis Telescopes (B. Namumba et al. 2019). For IC 1613, our H I mass of $(6.3 \pm 0.1) \times 10^7$ $M_\odot$ is 59% larger than the LITTLE THINGS value (D. A. Hunter et al. 2012), likely due to our inclusion of short-spacing data. Finally, in WLM, our H I mass of $(7.4 \pm 0.1) \times 10^7$ $M_\odot$ agrees within the uncertainty with LITTLE THINGS (D. A. Hunter et al. 2012) and is 9% larger than previous VLA measurements from A. A. Kepley et al. (2007). However, our VLA+GBT mass—similar to previous VLA measurements—is 31% smaller than the GBT flux measurements from D. A. Hunter et al. (2011) and 11% smaller than the GBT-only H I mass we measure here. Though

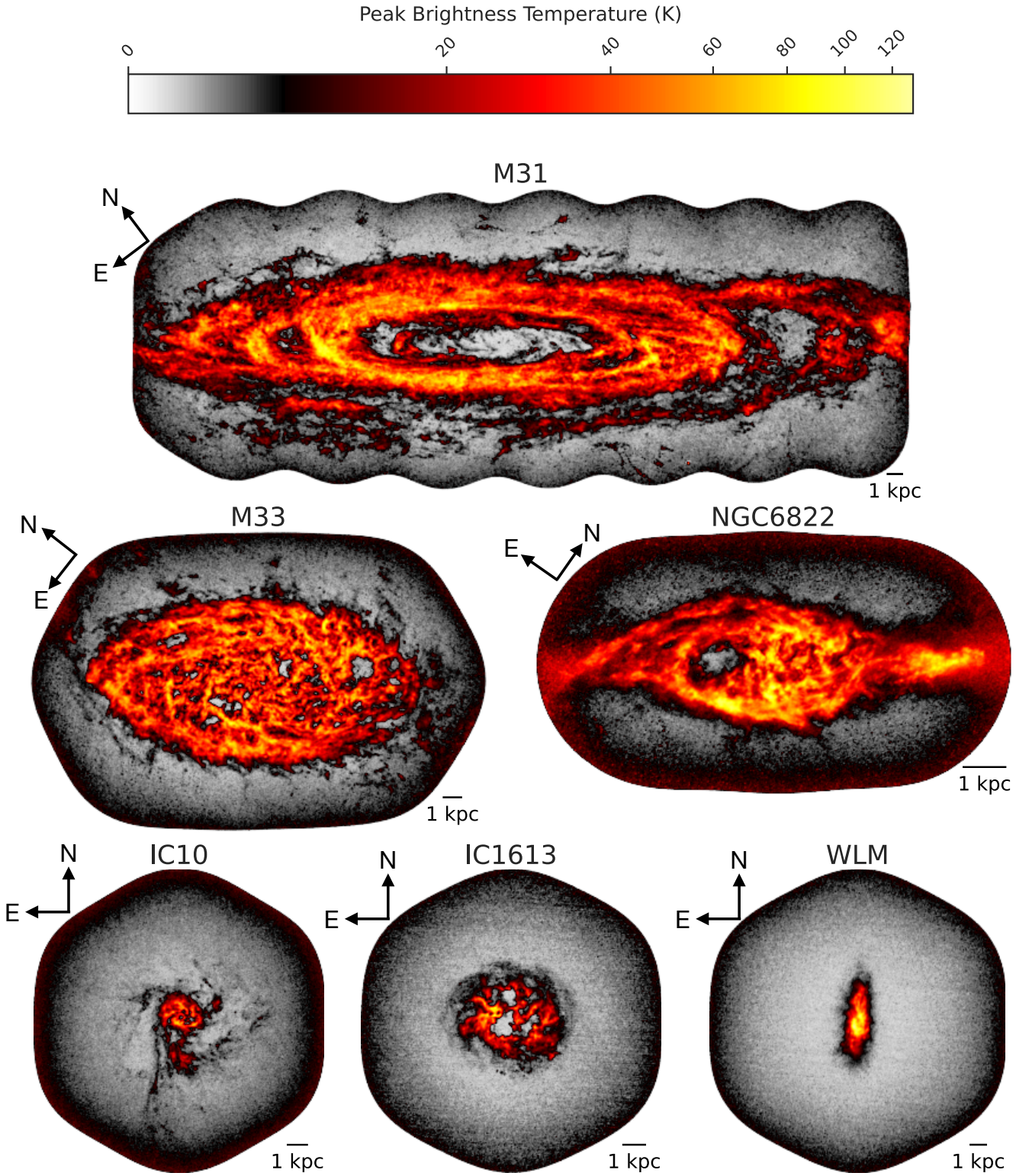

Figure 10. H I peak brightness temperature maps for combined CD and GBT imaging over the full LGLBS field of view for each target. The images show the extent of emission and complex morphology visible in the bright H I at high ∼100 pc resolution.

these single-dish H I masses are themselves discrepant, the consistently higher single-dish H I masses suggest a low-column density H I component that falls below the VLA sensitivity. Most of the previous VLA-based estimates tend to agree with our values, with the only exception being IC 1613, where the short-spacing correction drives the difference.

We note that some of our H I mass measurements differ from previous single-dish measurements despite the short-spacing corrections that we apply. Given our careful treatment for relative flux uncertainties prior to short-spacing correction (Appendix B) and our uniform calibration of the archival GBT observations (Appendix A), we are confident that the flux

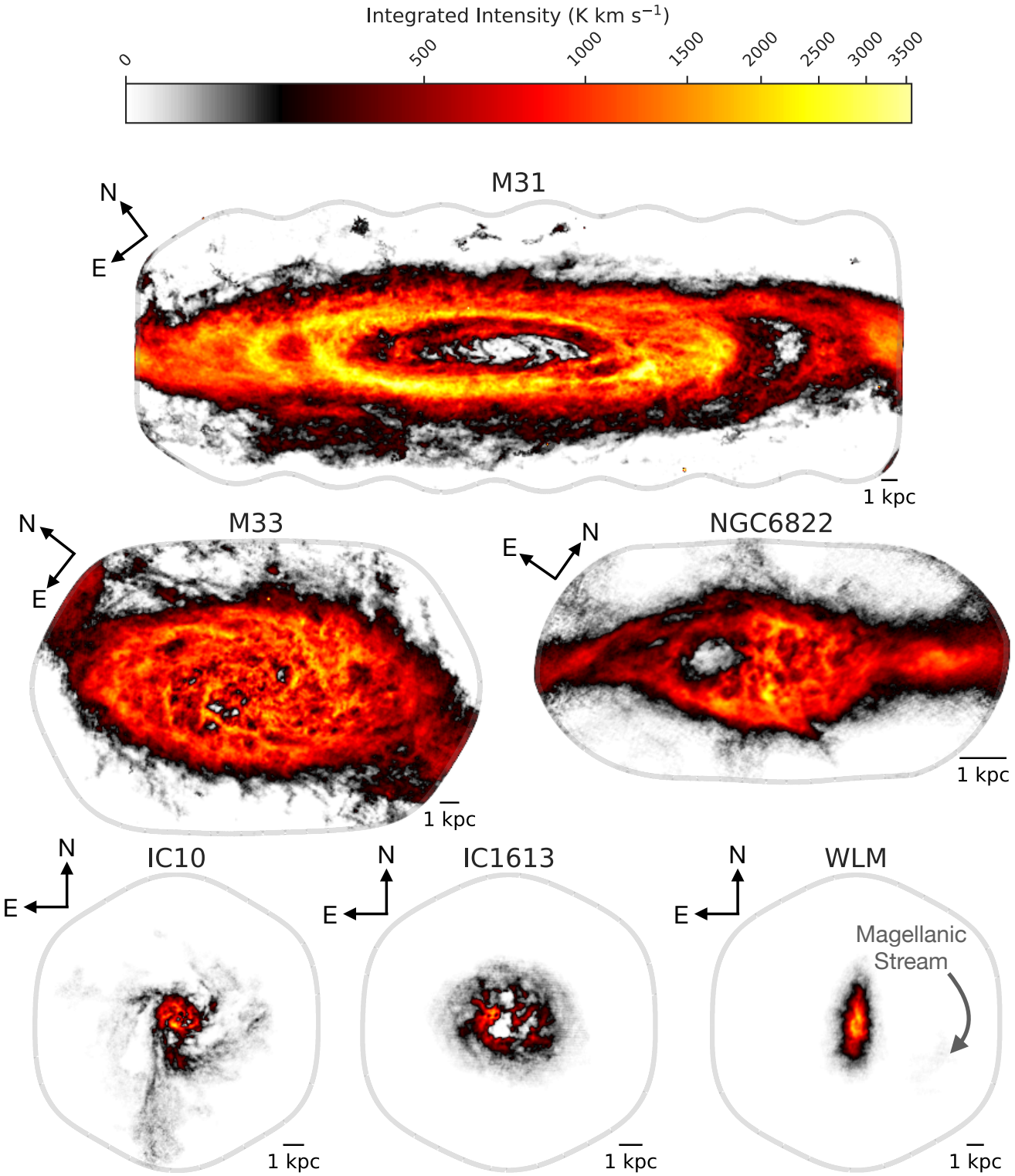

Figure 11. H I integrated intensity maps of the four LGLBS dwarf galaxy targets at their native angular resolution. These maps show the wide-field extent combining CD configuration and GBT observations. The morphology of the H I varies between these four galaxies, and we highlight in WLM where we recover faint H I emission from the edge of the foreground Magellanic Stream (M. E. Putman et al. 2003).

rescaling factors applied to the GBT cubes reflect our best total flux estimates when tied to the VLA absolute flux calibration. Therefore, we expect that the discrepant fluxes arise from differences in the spatial and spectral area used.

Over this small sample size of four dwarf galaxies, we see large variations in the gas morphology. IC 10 shows clear, >kpc-long extended H I structures whose morphology resembles tidal tails caused by a recent interaction (D. L. Nidever et al. 2013). NGC 6822 also shows an extended H I component relative to the compact stellar disk, which previous work has also suggested may be evidence of a tidal tail (W. J. G. de Blok & F. Walter 2006). In IC 1613, we do not detect extended H I

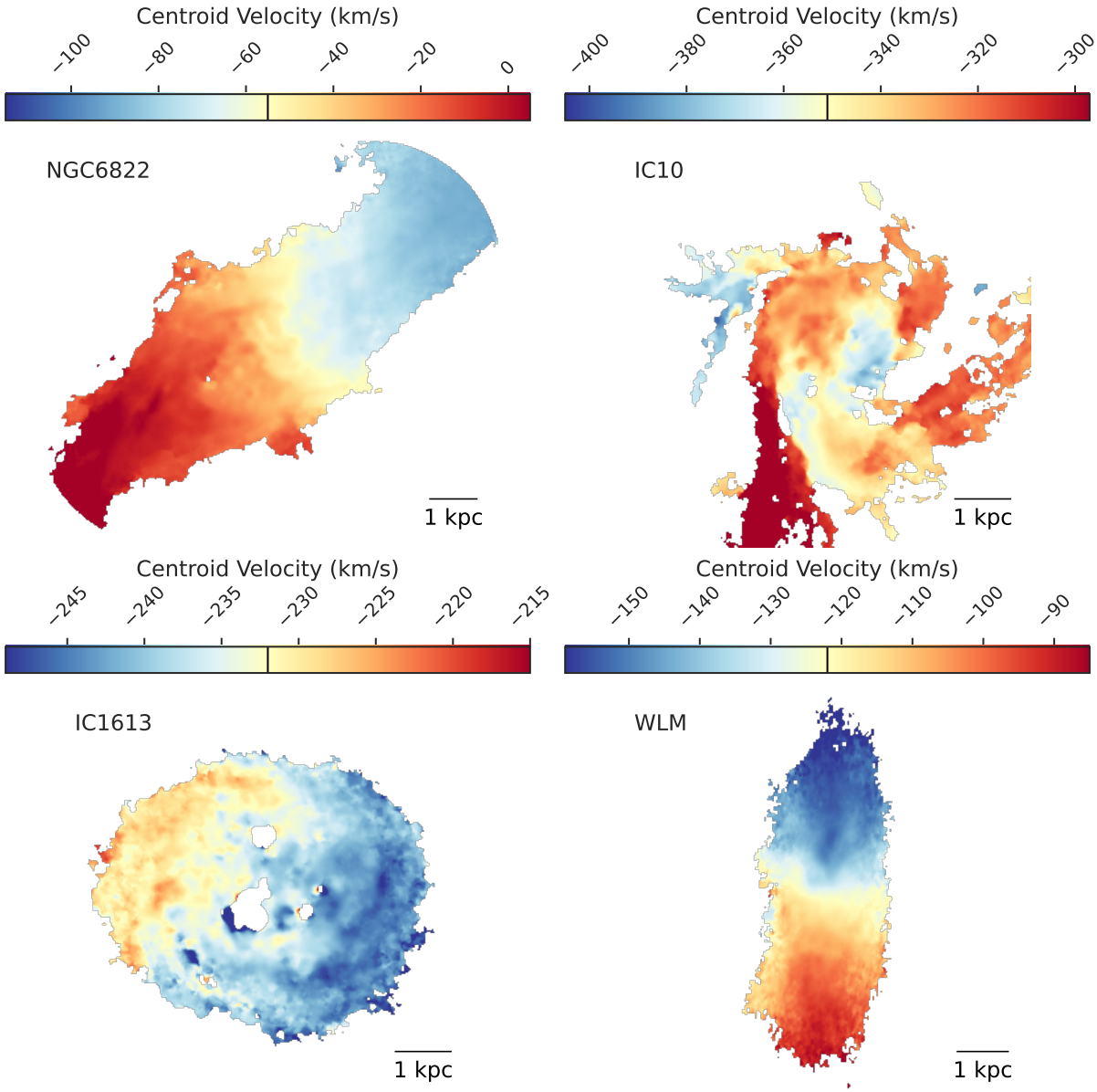

Figure 12. H I centroid velocity maps of the four LGLBS dwarf galaxies at a common physical resolution of 120 pc. The color maps are centered at the galaxy's systemic velocity indicated by the vertical black line in each color bar and extend to $\pm V_{\rm max}$ (the maximum rotation velocity). For IC 10, we show the velocity extent to $\pm 1.5 V_{\rm max}$ to better include the velocity ranges of the H I tidal tails.

emission above our column density sensitivity ($\sim$2–4 $\times$ 10^{19} cm^{-2}) beyond the galaxy disk. In WLM, a faint extended feature marked in Figure 11 corresponds to H I foreground emission associated with the Magellanic Stream (M. E. Putman et al. 2003), and we see weak filamentary structures extending beyond the disk (C. Vargas et al. 2025, in preparation). In both IC 1613 and WLM, the observed morphology mostly shows a rotating, inclined HI disk.

The H I kinematics (Figures 12 and 14) also show diversity and complexity. Visually, the inner disks of NGC 6822, IC 10, and WLM are relatively symmetric about the systemic velocity. This is expected for motions dominated by circular rotation and agrees well with previous H I kinematic modeling of these sources (S.-H. Oh et al. 2015; B. Namumba et al. 2017, 2019; R. Ianjamasimanana et al. 2020). On the other hand, IC 1613 appears to have an asymmetric velocity field about $V_{\rm sys}$.

Meanwhile, the centroid velocities in M31 and M33, shown in Figure 13, exhibit a typical circular-rotation pattern on large scales. Future LGLBS work will explore fine-scale kinematic variations and noncircular motions, leveraging our high angular and velocity resolution and building on the large body of literature dedicated to studying M31 and M33 (including E. Corbelli & S. E. Schneider 1997; E. Corbelli & P. Salucci 2000; E. Corbelli et al. 2010; S. Z. Kam et al. 2017; E. W. Koch et al. 2018b, and references in Table 2). Figure 13 also shows resolved H I detected well beyond the bright H I disks to the edges of the LGLBS's fields of view, where the H I kinematics offer potential new insight into the neutral gas being accreted or ejected. These extended "clouds" of H I have been studied in both galaxies (e.g., D. A. Thilker et al. 2004; T. Westmeier et al. 2005; M. E. Putman et al. 2009; O. C. Keenan et al. 2016; E. W. Koch et al. 2018b), but, for most of them, LGLBS will yield the highest resolution and

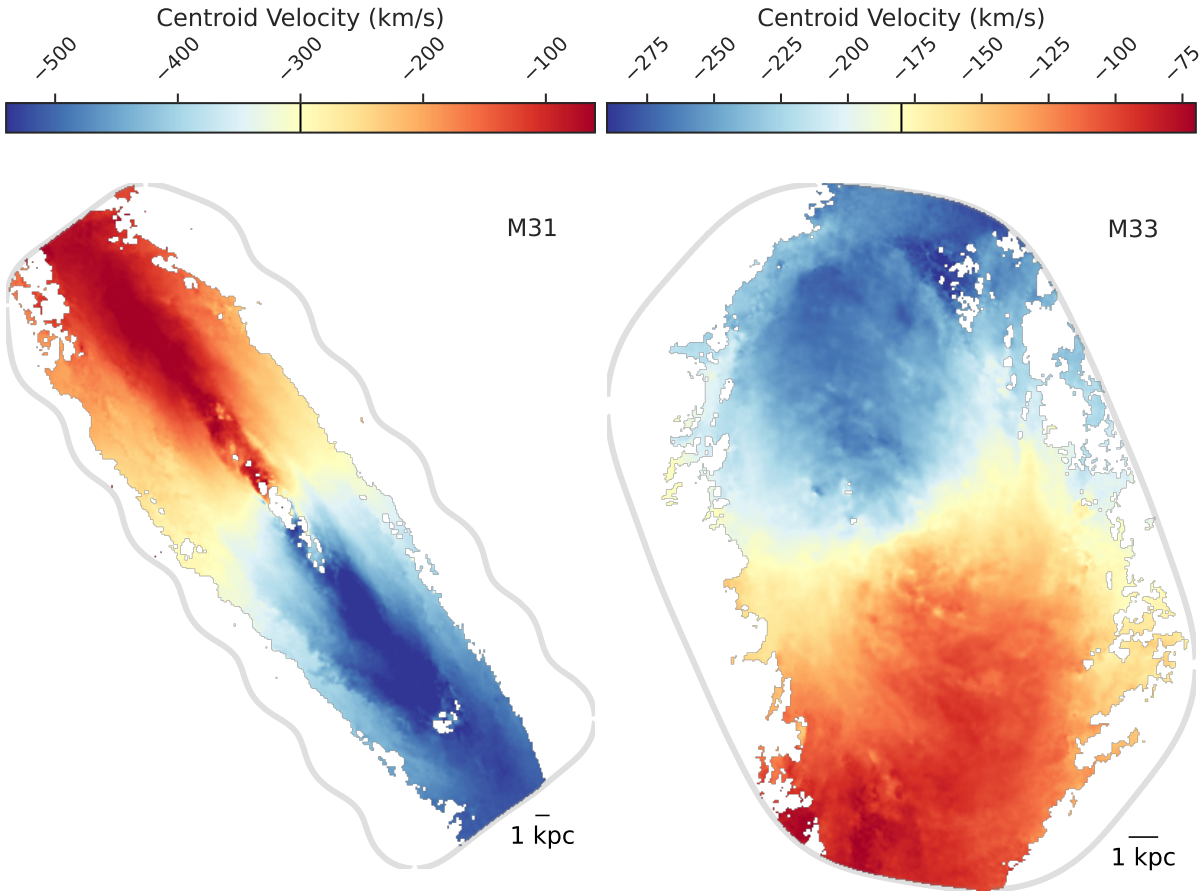

Figure 13. H I centroid velocity maps of M31 and M33 at a common physical resolution of 120 pc. The color maps are centered at the galaxy's systemic velocity indicated by the vertical black line in each color bar and extend to $\pm V_{\rm max}$ (the maximum rotation velocity).

most sensitive view to date, and often the first interferometric imaging.

In Figure 14, NGC 6822 and IC 10 show larger line widths in their inner disks (>10 km s^{-1}) compared to the other two targets. This likely reflects the combined effect of the disturbed H I environment from potential recent interactions and turbulent driving from massive stellar feedback. Both of these galaxies host massive star-forming regions, with IC 10 currently undergoing a localized starburst (D. A. Hunter 2001). Reflecting their morphology, ordered large-scale kinematics, and lower star formation rates, IC 1613 and WLM have lower line widths, though they do show localized enhancements in the vicinity of regions with known recent star formation. WLM's velocity dispersion is moderately larger than IC 1613's, which is expected due to our nearly edge-on view of WLM (R. Ianjamasimanana et al. 2020).

Figure 15 shows that M31 and M33 have regions with larger velocity dispersions (>15 km s^{-1}) than what we find in the four dwarf galaxies, consistent with previous work (E. W. Koch et al. 2018b; D. Utomo et al. 2019; E. W. Koch et al. 2021). These larger velocity dispersions result from several sources, including stellar feedback from wide-spread massive star formation that can drive elevated levels of turbulence (e.g., M.-M. Mac Low & R. S. Klessen 2004) and, particularly for M31, complex sight lines due to where multiple clouds are superimposed along the line of sight due to the high inclination angle. Using pilot LGLBS observations of M31 and M33, E. W. Koch et al. (2018b) and E. W. Koch et al. (2021) demonstrated that high-velocity resolution and sensitivity allow one to separate distinct kinematic features along individual lines of sight in these galaxies. A key focus of upcoming LGLBS work will be to conduct kinematics analyses that separate individual components to disentangle the different physical sources driving the complex H I line shapes.

These images provide a preview of the richness of the LGLBS H I maps. In terms of spatial resolution and sensitivity, LGLBS is a clear precursor to the H I mapping capabilities that SKA (R. Braun et al. 2015) and ngVLA (E. J. Murphy et al. 2018) will provide in the coming decades.

7. Summary and Outlook

We present the Local Group *L*-Band Survey (LGLBS), a Karl G. Jansky Very Large Array (VLA) program to image 21 cm H I and OH line emission and radio continuum from the six VLA-visible Local Group (all $D < 1$ Mpc) galaxies that show evidence for recent massive star formation and have H I mass $\log_{10}(M_{\rm HI}/M_\odot) > 7$. By focusing on these closest targets and using all four VLA configurations, we achieve an unprecedented combination of physical resolution and sensitivity. This paper presents the survey design, describes our calibration and quality assurance procedures, and shows some first results for imaging using the C and D configurations. Key points include the following:

1. The survey targets all H I-rich Local Group galaxies visible from the VLA site: the massive spiral M31

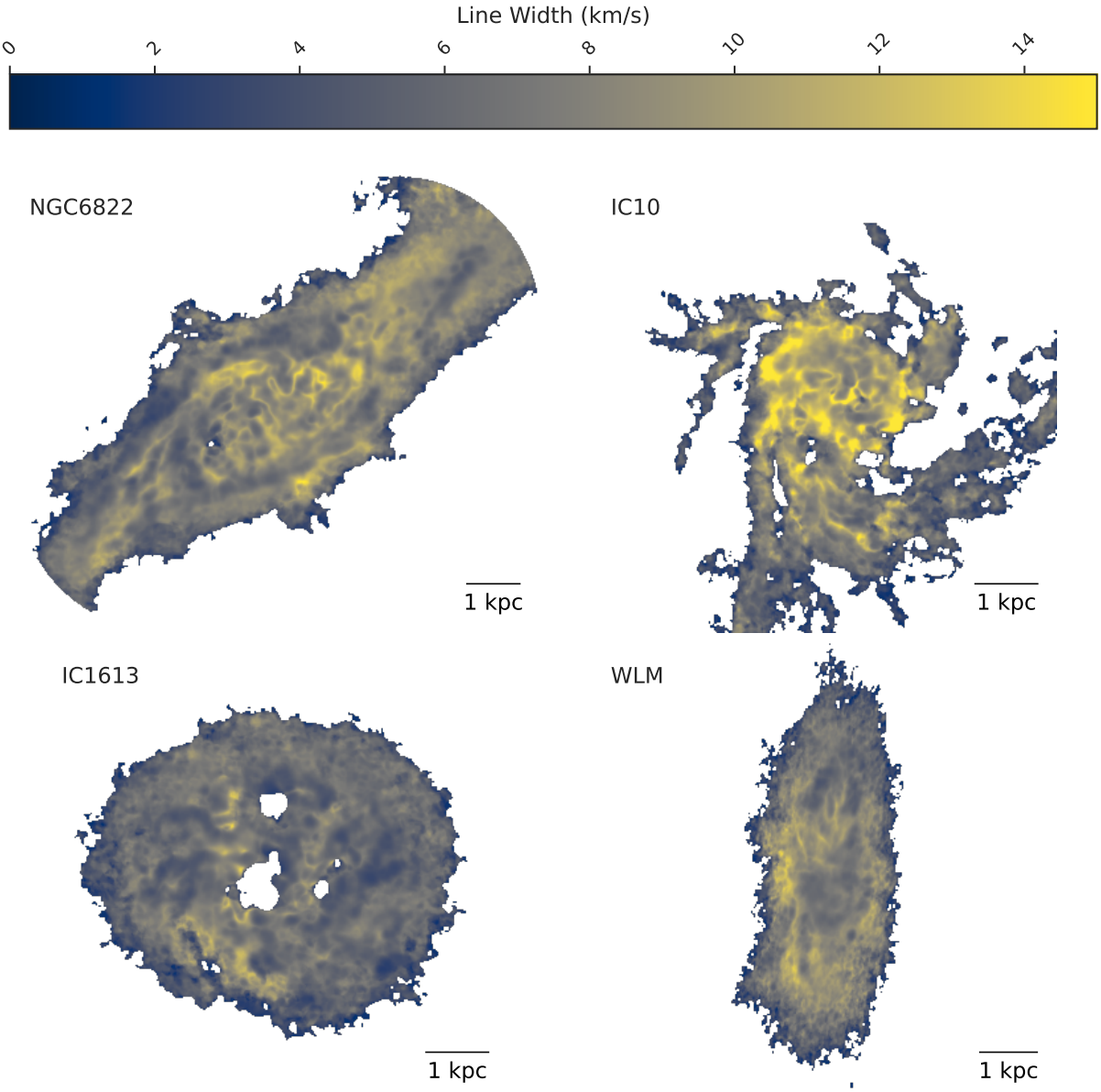

Figure 14. H I line width maps of the four LGLBS dwarf galaxies, as measured with the effective width, defined as $\sigma = I_{\rm HI}/\sqrt{2\pi}\ T_{\rm peak}$. Each map is shown at a common physical resolution of 120 pc. Regions with recent massive star formation in NGC 6822 and IC 10 tend to show larger velocity dispersions, while IC 1613 and WLM with lower recent star formation rates tend to have lower dispersions.

(Andromeda), the dwarf spiral M33 (Triangulum), and the four dwarf irregulars IC 10, IC 1613, NGC 6822, and WLM. Our survey complements the ongoing GASKAP-HI survey (N. M. Pingel et al. 2022), which will produce similar-quality data for the LMC and SMC.

2. We take advantage of the VLA's powerful WIDAR correlator to simultaneously observe the 21 cm line at sharp 0.4 km s^{-1} velocity resolution, the full 1–2 GHz polarized continuum, and the OH lines at 1612, 1665, 1667, and 1720 MHz (Figure 4). We also record information on radio recombination lines and enabled simultaneous REALFAST observations by another team to search for transients such as FRBs (C. J. Law et al. 2018). The 21 cm observations trace emission and absorption from atomic gas, which makes up most of the ISM in each of our targets. The continuum observations mostly trace a mixture of free–free emission associated with H II regions, synchrotron emission powered by current and past SNRs, and background sources. The OH main lines (1667, 1665 MHz) provide a faint but potentially powerful probe of the molecular ISM that complements CO and dust emission (M. P. Busch 2024), while the OH satellite lines (1612, 1720 MHz) can exhibit strong masers from the ISM, which probe physical conditions of shocked gas or stellar activity (P. Lockett et al. 1999; M. D. Gray et al. 2005; E. Koch et al. 2018a).
3. Our observations cover the area of high column density H I and star formation activity in each target, and we observe each target using each of the VLA's four configurations (A, B, C, and D). This combination yields 21 cm maps with physical resolutions as high as 10–20 pc and continuum maps with resolution as high as 5–10 pc. Combined with our 0.4 km s^{-1} channel width, LGLBS

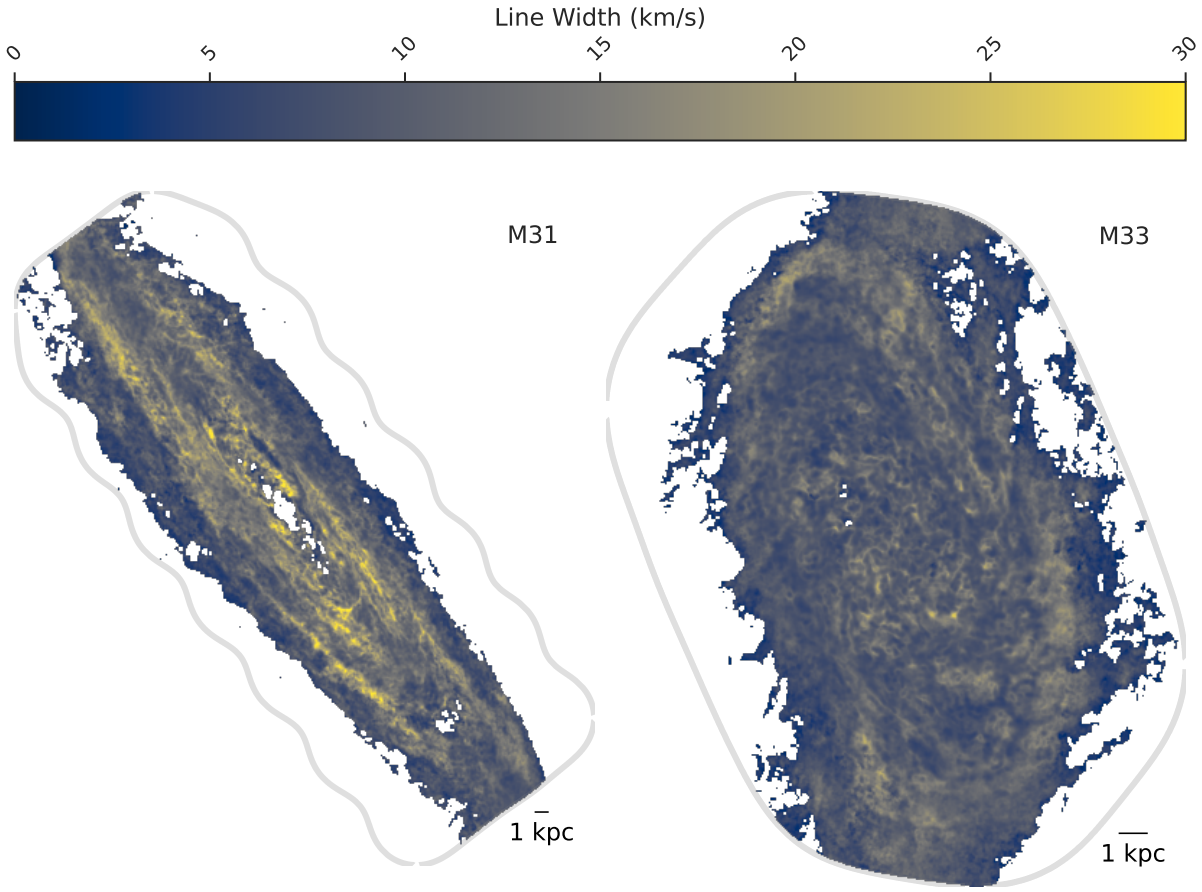

Figure 15. H I line width maps of M31 and M33, as measured with the effective width, defined as $\sigma = I_{\rm HI}/\sqrt{2\pi}\ T_{\rm peak}$. Each map is shown at a common physical resolution of 120 pc. Both M31 and M33 have regions of larger line widths relative to the dwarf galaxies (Figure 14), with the largest line widths in M31 likely resulting from multiple components along single sight lines from its high inclination angle (e.g., R. Braun et al. 2009; L. Chemin et al. 2009; E. W. Koch et al. 2021).

Table 5
21 cm H I Imaging at 120 pc Resolution and H I Masses from Combined VLA+GBT and GBT-only

Galaxy	Synthesized Beam (arcsec)	$M_{\rm HI}$ (VLA+GBT) ($M_\odot$) ($M_\odot$)	$M_{\rm HI}$ (GBT-only)[c] ($M_\odot$) ($M_\odot$)	5σ H I Column Density[a] ($\rm cm^{-2}$)	5σ H I Mass per Beam[a] ($M_\odot$)
M31[b]	32	$(5.7 \pm 0.1 \pm 0.3) \times 10^9$	$(5.6 \pm 0.1 \pm 0.3) \times 10^9$	3.1×10^{19}	4.1×10^3
M33[b]	28	$(2.0 \pm 0.1 \pm 0.1) \times 10^9$	$(2.0 \pm 0.1 \pm 0.1) \times 10^9$	2.2×10^{19}	2.9×10^3
IC 10	31	$(7.5 \pm 0.1 \pm 0.4) \times 10^7$	$(7.7 \pm 0.1 \pm 0.3) \times 10^7$	2.3×10^{19}	2.9×10^3
IC 1613	33	$(6.3 \pm 0.1 \pm 0.3) \times 10^7$	$(6.3 \pm 0.1 \pm 0.3) \times 10^7$	1.8×10^{19}	2.3×10^3
NGC 6822[b]	48	$(1.9 \pm 0.1 \pm 0.1) \times 10^8$	$(1.8 \pm 0.1 \pm 0.1) \times 10^8$	1.4×10^{19}	1.8×10^3
WLM	27	$(7.4 \pm 0.1 \pm 0.4) \times 10^7$	$(8.2 \pm 0.1 \pm 0.4) \times 10^7$	4.1×10^{19}	3.9×10^3

Notes. Total H I mass, 5σ column density, and mass per beam sensitivities measured on matched 120 pc scales from CD configuration imaging combined with GBT short-spacing data. The two uncertainties for the mass values correspond to the statistical and systematic uncertainty, respectively, where we assume a systematic uncertainty of 5% from flux uncertainty.
[a] The 5σ H I column density and mass sensitivities are measured over 10 km $\rm s^{-1}$.
[b] Our VLA+GBT mass measurements are limited by the LGLBS spatial coverage.
[c] GBT mass measurements are made at the native GBT resolution over a field of view that extends beyond the VLA coverage. These masses also incorporate the flux calibration corrections derived for feathering in Appendix B.

achieves a detailed radio view of the atomic gas, H II regions, and SNRs previously only accessible in the Milky Way.

4. As of this publication, all observations have concluded and >430 tracks ($\gtrsim$1800 hr of observations) have been calibrated and manually quality assured. We present a new software framework that enables this QA. The framework deploys a slightly modified version of the VLA pipeline to calibrate each track and then produces a series of interactive plots that allow for in-depth inspection of the visibility data using a browser-based interface. This framework allowed our distributed team to efficiently QA a large amount of data. The approach is scalable and can be adapted for use in other projects dealing with widely distributed collaborations and large data volumes and is readily applicable to non-LGLBS

VLA *L*-band observations taken with the WIDAR correlator. We make our code publicly available via the `ReductionPipeline`[43] and `QAPlotter`[44] packages.

5. We present the first 21 cm images for our six targets using data from the compact C+D configurations, combined with GBT short-spacing data. These show good overall agreement with previous large-scale measurements, reveal extended atomic gas distributions down to column densities of $\approx$2–4 $\times$ 10^{19} cm^{-2} (5σ), and 5σ sensitivity to individual H I clouds with masses as low as $\gtrsim$2–5 $\times$ 10^3 $M_\odot$.

Even after calibration and quality assurance, imaging the data represents a significant technical challenge. The 21 cm imaging for our combined ABCD data is described in detail by N. Pingel et al. (2025, in preparation; and see N. M. Pingel et al. 2024), while the Stokes*I* continuum imaging is described by S. Sarbadhicary et al. (2025, in preparation). All images and data cubes from LGLBS will be publicly available, with the CD+GBT data presented in this paper publicly released at doi:10.11570/25.0076, and initial data releases of the high-resolution line and continuum data will accompany the continuum and line imaging papers.

Acknowledgments

We gratefully acknowledge the anonymous reviewer for providing comments that improved the clarity of this paper. We are grateful for the support of the staff at the National Radio Astronomy Observatory who facilitated this "Extra Large" program. Our survey design benefited from an extensive technical review led by Claire Chandler, and we are grateful for the work of the VLA scheduling team, especially Amy Mioduszewski, for helping facilitate our observational requirements. We thank Filippo Maccagni for sharing his compilation of archival H I surveys that we reproduce in Figure 3. The National Radio Astronomy Observatory is a facility of the National Science Foundation operated under cooperative agreement by Associated Universities, Inc. This research was enabled in part by support provided by the Digital Research Alliance of Canada (alliancecan.ca). This research used the Canadian Advanced Network For Astronomy Research (CANFAR) operated in partnership by the Canadian Astronomy Data Centre and The Digital Research Alliance of Canada with support from the National Research Council of Canada the Canadian Space Agency, CANARIE, and the Canadian Foundation for Innovation. Some of the computations in this paper were conducted on the Smithsonian High Performance Cluster (SI/HPC), Smithsonian Institution (https://doi.org/10.25572/SIHPC). The LGLBS collaboration is grateful for support from the National Science Foundation, AST-2205628 and AST-205630. E.W.K. acknowledges support from the Smithsonian Institution as a Submillimeter Array (SMA) Fellow and the Natural Sciences and Engineering Research Council of Canada. L.C. also acknowledges support from NSF grant AST-2107070. E.R. and H.C. acknowledge the support of the Natural Sciences and Engineering Research Council of Canada (NSERC), funding reference No. RGPIN-2022-03499. T.W. gratefully acknowledges support from the Chu Family Foundation for the Vermilion River Fund for Astronomical Research at the University of Illinois. S.S. gratefully acknowledges support provided by the University of Wisconsin - Madison Office of the Vice Chancellor for Research and Graduate Education with funding from the Wisconsin Alumni Research Foundation. D.J.P. is supported through the South African Research Chairs Initiative of the Department of Science and Technology and National Research Foundation (grant No. 77825). J.S. acknowledges support by the National Aeronautics and Space Administration (NASA) through the NASA Hubble Fellowship grant HST-HF2-51544 awarded by the Space Telescope Science Institute (STScI), which is operated by the Association of Universities for Research in Astronomy, Inc., under contract NAS 5-26555.

Facilities: VLA, GBT.

Software: astropy (Astropy Collaboration et al. 2013, 2018, 2022), plotly, radio-astro-tools (spectral-cube, radio-beam, uvcombine) (A. Ginsburg et al. 2019), CASA (CASA Team et al. 2022), GBTIDL (P. Marganian et al. 2013), seaborn (M. Waskom et al. 2017), matplotlib (J. D. Hunter 2007), numpy & scipy (P. Virtanen et al. 2020), PHANGS imaging pipeline (A. K. Leroy et al. 2021).

Appendix A
GBT Calibration and Imaging

The H I emission in our targets is extended relative to both the VLA primary beam and the largest recoverable spatial scales in D configuration. Thus, we require short-spacing corrections with single-dish observations to capture the large-scale H I emission. For this purpose, we use archival GBT data from several observing projects. Most used the now-decommissioned GBT Spectrometer backend, while some later projects used the Versatile GBT Astronomical Spectrometer (VEGAS).

We re-reduced the GBT spectrometer data from Green Bank Observatory projects AGBT12B_312 (PI: Johnson, targets: WLM and IC 10), AGBT13A_430 (PI: Ashley, target: IC 10), and AGBT13B_169 (PI: Johnson, target: NGC 6822). The observations, GBT spectrometer setup, and observing strategy are similar to what is described in M. Johnson (2013). In brief, the total bandwidth was 12.5 MHz with 16,384 channels, and the band centered on the frequency of the H I line at the heliocentric redshifts of the sources. For calibration purposes, the band was frequency-switched -3.5 MHz from the center frequency with a 1 s period. We re-reduce the spectrometer spectra using the `getfs` procedure in the GBTIDL[45] data reduction package. We then fit and subtract a second-order polynomial baseline across emission-free channels to account for any residual structure and remove continuum after the `getfs` procedure. The spectra are scaled assuming a constant zenith opacity of 0.01 to convert into units of opacity-corrected antenna temperature (T_A^*). These calibrated spectra are smoothed to a final resolution of 5.15 km s^{-1} using a Gaussian kernel.

The VEGAS setup and observing strategy for AGBT16A_413 (PI: Pisano) targeting IC 1613 is similar to that outlined in N. M. Pingel et al. (2018). The total bandwidth was 23.44 MHz with 32,768 channels with the band centered on the H I line at the heliocentric redshifts of the source. The band was frequency-switched by $\pm$5.5 MHz. Note that N. M. Pingel et al. (2018)

[43] https://github.com/LocalGroup-VLALegacy/ReductionPipeline
[44] https://github.com/LocalGroup-VLALegacy/QAPlotter
[45] https://gbtidl.nrao.edu/

presented the details on the flux calibration procedure, including the custom GBTIDL routines that build a reference spectrum from the first four and last four integrations at the edge of the $2^\circ \times 2^\circ$ on-the-fly maps. Additionally, they accounted for a crosstalk issue in the backend electronics that was present in the early VEGAS science data and affects the flux calibration. To convert to units of (T_A^*), we use the same scaling and baseline fitting procedure as described above for the GBT spectrometer data, and also smooth these data to a final spectral resolution of 5.15 km s^{-1}.

Before imaging, we resample the spectral data onto a common grid using the `gshift` GBTIDL procedure. We also convert the Galactic coordinates in the headers of the spectrometer SDFITS files[46] to J2000 equatorial coordinates. The data are then combined and imaged using the `gbtgridder`[47] tool. We adopt a gain of 1.86 K Jy^{-1}, based on detailed modeling of the aperture illumination of the GBT at the *L* band, and assume the FWHM of the GBT *L* band beam to be 9.′1 (N. M. Pingel et al. 2018; A. Sardone et al. 2021).

Appendix B
Relative Flux Calibration for H I Short-spacing Correction

To ensure consistency when combining the interferometer and single-dish data, we test whether the absolute flux calibrations agree within the angular scales measured by both data sets. For these tests, we focus on VLA data in the C and D configurations, i.e., those with the shortest baseline coverage and largest overlap with GBT in angular scales sampled.

Prior to comparing the flux at common angular scales, we smooth (if necessary) and resample the GBT cubes to the 4.1 km s^{-1} of our "low spectral resolution" VLA H I cubes. We then check the spatial registration of the VLA to these velocity-matched GBT cubes with the `image_registration` package (A. Ginsburg et al. 2014). We find spatial offsets consistent within <20% of the GBT beam size and therefore apply no spatial shifts to the GBT cubes. Finally, we reproject the GBT cubes to the same spatial pixel grid as the VLA data.

We use the `uvcombine` package (E. Koch & A. Ginsburg 2022) and apply a similar set of tests as described in E. W. Koch et al. (2018b), which are based on S. Stanimirovic et al. (1999). Using the reprojected GBT cubes, we sample the data on angular scales between 9.′5 and 18′, corresponding to baseline lengths of 100–40 m, and aggregate the distribution of flux measurements over the H I velocity range for each target. Following E. W. Koch et al. (2018b), we model the natural log of the flux ratios with a Cauchy distribution, which naturally accounts for excess tails in the distribution that result from noise fluctuations in either the numerator or denominator of the ratio. We fit this model to the measured flux ratios using a maximum-likelihood approach. The location of the peak in the best-fit model corresponds to the interferometer-to-single-dish flux scaling factor. Table 6 gives the fitted flux scaling factors and the velocity range to which the flux ratios are fit.

We note that the M33 flux ratio value of 1.10 given in Table 6 is larger than the value of 1.02 from E. W. Koch et al. (2018b), despite using the same GBT data. The gridded GBT data have a larger effective beamwidth of 9.′8, as they were gridded with a Gaussian kernel, not the Gaussian-Bessel kernel, to account for the minimal spatial overlap between the four observed maps (see further details in F. J. Lockman et al. 2012). We perform the same series of checks from E. W. Koch et al. (2018b) and find no other systematic effects to explain this discrepancy in the flux ratio value. After thorough checks, we find that this difference persists primarily from the inclusion of the LGLBS D configuration observations significantly increasing the short baseline coverage relative to E. W. Koch et al. (2018b) that used only a subset of the C configuration data included here. As including the D configuration is ideal for these *uv*-overlap tests, we adopt the new flux ratio of 1.10 here.

Table 6
Fitted VLA-to-GBT Flux Scaling Factors Applied to the GBT H I Cubes Prior to Short-spacing Correction with Feathering

Galaxy	GBT Flux Scaling Factor	Velocity Range (km s^{-1})
M31	1.00	−500 to −100
M33	1.10	−260 to −100
NGC 6822	0.92	−75 to −25
IC 10	0.96	−380 to −260
IC 1613	0.89	−265 to −210
WLM	1.14	−170 to −70

Note. The velocity range indicates the spectral channels incorporated into the scaling factor measurement.

Table 6 shows the fitted flux scaling factors, which we apply to the GBT data before feathering. Similar to previous work, we adopt the VLA flux calibration as the reference and apply correction factors to only the GBT data. The scaling factors in Table 6 tend to be within 10% of unity, and thus appear broadly consistent with the expected systematic uncertainty in the flux calibration of both data sets. The values we find are typical from studies using similar combinations of VLA and GBT data with various other telescopes (e.g., K. Blagrave et al. 2017; E. W. Koch et al. 2018b, 2021).

Although we derive these flux scaling factors using only the compact VLA C and D configurations, we use them for all VLA+GBT combinations. The extended VLA configurations will be on a consistent R. A. Perley & B. J. Butler (2017) flux scale with the C and D configurations.

Appendix C
Modeling and Separating the Galactic H I Foreground in NGC 6822

NGC 6822 has significant velocity overlap with Galactic H I near recession velocity 0 km s^{-1}. The foreground H I is bright and extended relative to the VLA primary beam due to a foreground Galactic molecular cloud (P. Gratier et al. 2010a). To separate the foreground H I emission spatially overlapping with NGC 6822, we developed a new approach that utilizes the local pixel-wise infilling (LPI) technique developed by A. K. Saydjari & D. P. Finkbeiner (2022) to allow for photometry on structured backgrounds.

First, we use the rotation curve model derived in B. Namumba et al. (2017) to spatially mask NGC 6822 in the GBT cube. To extrapolate the rotation curve beyond radii included in their measurements, we fit an arctan function to their circular-rotation data. We find that some H I emission in these outer regions deviates from the single orientation (inclination/positions angle) of the NGC 6822 rotation curve from

[46] https://fits.gsfc.nasa.gov/registry/sdfits.html
[47] https://github.com/GreenBankObservatory/gbtgridder

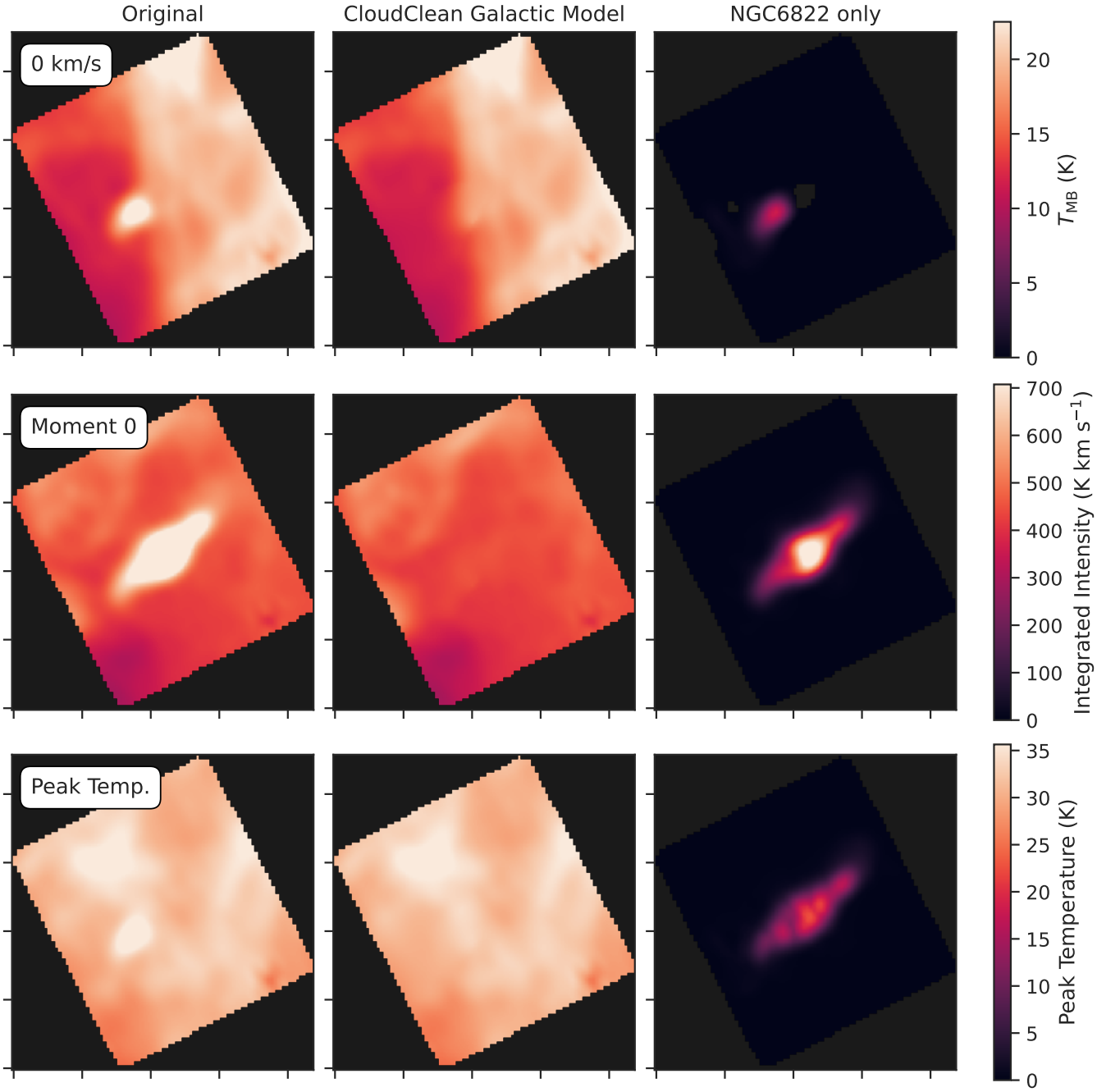

Figure 16. Foreground Galactic H I separation in NGC 6822 using `CloudClean.jl` (A. K. Saydjari & D. P. Finkbeiner 2022). We show the original GBT cube (left column), the Galactic H I–only model produced with `CloudClean.jl` (center column), and the NGC 6822–only cube from subtracting the Galactic model from the original (right column). The rows show a single channel at recession velocity 0 km s^{-1} (top row), integrated intensity (moment 0; middle row), and peak temperature (bottom row). LPI shows excellent results for separating Galactic H I foreground from NGC 6822 emission where both overlap in velocity.

B. Namumba et al. (2017) and is thus not included in the mask. To account for this deviation, we simply extend the mask, at all radii, spectrally by ± 20 km s^{-1} and spatially by 1 beamwidth using binary dilation. We do not apply this binary dilation operation for velocity channels between -5 to 20 km s^{-1} where we visually confirm that all NGC 6822 emission is contained within the original nondilated mask. In those channels, we do not apply any spatial extension of the mask. We note that these kinematics deviations that are recovered in our resolved, deep H I observations will be explored with updated circular-rotation curve modeling in future work. For our purposes here, however, it is sufficient to overly mask to ensure that the mask thoroughly excludes all H I emission from NGC 6822, even if some Galactic H I emission is included in the mask. We visually inspect the GBT cube after masking NGC 6822 to ensure that only Galactic H I emission remains.

We then build a covariance matrix from the remaining purely Galactic H I emission and infill the masked region in each channel using LPI implemented in `CloudClean.jl`.[48] We build a local covariance matrix of size 129 × 129 and an infill region size of 51 pixels, matching the largest masked area (in the NGC 6822 GBT data cube, 1 pixel has linear size 3.′5).

[48] https://github.com/andrew-saydjari/CloudClean.jl

We infill the masked regions using the mean LPI distribution in each channel. We then subtract the infilled Galactic H I cube from the original GBT cube to produce an NGC 6822–only H I cube. We use this cube for the feathering described above in Appendix B, though note that the infill modeling does not affect the relative flux calibration measurement because we use channels without strong foreground H I for the flux calibration comparison.

Figure 16 shows the infill results in one channel, the integrated intensity map, and the peak temperature map for the original data set, the Galactic H I–only model from `CloudClean.jl`, and the final NGC 6822–only cube. LPI produces an excellent foreground H I model, which, when subtracted from the original cube, leaves behind only the emission from NGC 6822.

From the NGC 6822–only cube, adopting a distance of 526 ± 25 kpc (A. J. Lee et al. 2024; see Table 1), we measure a total luminosity of $(1.21 \pm 0.06) \times 10^{10}$ K km s^{-1} pc^2 or an optically thin H I mass of $(1.8 \pm 0.1) \times 10^8$ $M_\odot$, which includes the flux scaling correction factor of 0.92 (see Appendix B). This H I mass is 20% larger than the total H I mass of 1.5×10^8 $M_\odot$ measured with Parkes observations by W. J. G. de Blok & F. Walter (2006, adjusting for a distance of 520 kpc that we adopt here). This small increase likely results from our pixel-wise infilling approach to modeling the Galactic H I, as the interpolation scheme used by W. J. G. de Blok & F. Walter (2006) will produce an overly smoothed version of the Galactic H I foreground.

While most foreground Galactic H I is filtered out by the VLA, some fine-scale extended H I filaments that are clearly visible in the GBT map are still detected in the C+D cubes at recession velocities of ∼−30–10 km s^{-1}. These are spatially separated from NGC 6822's redshifted limb, and we manually mask this emission prior to calculating H I properties and moment maps. The result of this combined LPI and manual masking leads to a data cube containing our best estimate of emission only from NGC 6822.

ORCID iDs

Eric W. Koch https://orcid.org/0000-0001-9605-780X
Adam K. Leroy https://orcid.org/0000-0002-2545-1700
Erik W. Rosolowsky https://orcid.org/0000-0002-5204-2259
Laura Chomiuk https://orcid.org/0000-0002-8400-3705
Julianne J. Dalcanton https://orcid.org/0000-0002-1264-2006
Nickolas M. Pingel https://orcid.org/0000-0001-9504-7386
Sumit K. Sarbadhicary https://orcid.org/0000-0002-4781-7291
Snežana Stanimirović https://orcid.org/0000-0002-3418-7817
Fabian Walter https://orcid.org/0000-0003-4793-7880
Haylee N. Archer https://orcid.org/0000-0002-8449-4815
Alberto D. Bolatto https://orcid.org/0000-0002-5480-5686
Michael P. Busch https://orcid.org/0000-0003-4961-6511
Hongxing Chen https://orcid.org/0009-0005-1781-5665
Ryan Chown https://orcid.org/0000-0001-8241-7704
Harrisen Corbould https://orcid.org/0009-0007-7949-6633
Serena A. Cronin https://orcid.org/0000-0002-9511-1330
Jeremy Darling https://orcid.org/0000-0003-2511-2060
Thomas Do https://orcid.org/0000-0001-6105-7308
Jennifer Donovan Meyer https://orcid.org/0000-0002-3106-7676
Cosima Eibensteiner https://orcid.org/0000-0002-1185-2810
Deidre Hunter https://orcid.org/0000-0002-3322-9798
Rémy Indebetouw https://orcid.org/0000-0002-4663-6827
Preshanth Jagannathan https://orcid.org/0000-0002-5825-9635
Amanda A. Kepley https://orcid.org/0000-0002-3227-4917
Chang-Goo Kim https://orcid.org/0000-0003-2896-3725
Shin-Jeong Kim https://orcid.org/0000-0002-6760-7531
Timea O. Kovacs https://orcid.org/0000-0001-6649-8559
Joshua Marvil https://orcid.org/0000-0003-1111-8066
Eric J. Murphy https://orcid.org/0000-0001-7089-7325
Claire E. Murray https://orcid.org/0000-0002-7743-8129
Jürgen Ott https://orcid.org/0000-0001-8224-1956
D.J. Pisano https://orcid.org/0000-0001-7996-7860
Mary Putman https://orcid.org/0000-0002-1129-1873
Daniel R. Rybarczyk https://orcid.org/0000-0003-3351-6831
Julia Roman-Duval https://orcid.org/0000-0001-6326-7069
Karin Sandstrom https://orcid.org/0000-0002-4378-8534
Eva Schinnerer https://orcid.org/0000-0002-3933-7677
Evan D. Skillman https://orcid.org/0000-0003-0605-8732
Adam Smercina https://orcid.org/0000-0003-2599-7524
Ioana Stelea https://orcid.org/0000-0002-4110-8769
Jay Strader https://orcid.org/0000-0002-1468-9668
Jiayi Sun https://orcid.org/0000-0003-0378-4667
Devisree Tallapaneni https://orcid.org/0009-0000-2209-7972
Elizabeth Tarantino https://orcid.org/0000-0003-1356-1096
Vicente Villanueva https://orcid.org/0000-0002-5877-379X
Daniel R. Weisz https://orcid.org/0000-0002-6442-6030
Thomas G. Williams https://orcid.org/0000-0002-0012-2142
Tony Wong https://orcid.org/0000-0002-7759-0585

References

Abbott, T. M. C., Abdalla, F. B., Allam, S., et al. 2018, ApJS, 239, 18
Allen, R. J., Le Bourlot, J., Lequeux, J., Pineau des Forets, G., & Roueff, E. 1995, ApJ, 444, 157
Anderson, L. D., Bania, T. M., Balser, D. S., et al. 2014, ApJS, 212, 1
Anna-Thomas, R., Law, C. J., Koch, E. W., et al. 2025, arXiv:2503.02947
Astropy Collaboration, Price-Whelan, A. M., Lim, P. L., et al. 2022, ApJ, 935, 167
Astropy Collaboration, Price-Whelan, A. M., Sipőcz, B. M., et al. 2018, AJ, 156, 123
Astropy Collaboration, Robitaille, T. P., Tollerud, E. J., et al. 2013, A&A, 558, A33
Azimlu, M., Marciniak, R., & Barmby, P. 2011, AJ, 142, 139
Beck, R. 2015, A&ARv, 24, 4
Beck, R., Berkhuijsen, E. M., & Hoernes, P. 1998, A&AS, 129, 329
Beck, R., Loiseau, N., Hummel, E., et al. 1989, A&A, 222, 58
Berezhko, E. G., & Völk, H. J. 2004, A&A, 427, 525
Besla, G., Kallivayalil, N., Hernquist, L., et al. 2012, MNRAS, 421, 2109
Beuther, H., Bihr, S., Rugel, M., et al. 2016, A&A, 595, A32
Blagrave, K., Martin, P. G., Joncas, G., et al. 2017, ApJ, 834, 126
Braun, R. 1990a, ApJS, 72, 761
Braun, R. 1990b, ApJS, 72, 755
Braun, R., Bourke, T., Green, J. A., Keane, E., & Wagg, J. 2015, in Proc. Advancing Astrophysics with the Square Kilometre Array (AASKA14) (Trieste: SISSA), 174
Braun, R., & Thilker, D. A. 2004, A&A, 417, 421
Braun, R., Thilker, D. A., Walterbos, R. A. M., & Corbelli, E. 2009, ApJ, 695, 937
Bresolin, F., Urbaneja, M. A., Gieren, W., Pietrzyński, G., & Kudritzki, R.-P. 2007, ApJ, 671, 2028
Brinks, E., & Shane, W. W. 1984, A&AS, 55, 179
Brown, R. L., Lockman, F. J., & Knapp, G. R. 1978, ARA&A, 16, 445
Busch, M. P. 2024, ApJ, 967, 148
Carilli, C. L., & Walter, F. 2013, ARA&A, 51, 105
CASA Team, Bean, B., Bhatnagar, S., et al. 2022, PASP, 134, 114501
Chemin, L., Carignan, C., & Foster, T. 2009, ApJ, 705, 1395
Chiang, I.-D., Sandstrom, K. M., Chastenet, J., et al. 2021, ApJ, 907, 29
Chomiuk, L., & Wilcots, E. M. 2009, ApJ, 703, 370
Chung, A., van Gorkom, J. H., Kenney, J. D. P., Crowl, H., & Vollmer, B. 2009, AJ, 138, 1741
Condon, J. J. 1992, ARA&A, 30, 575
Corbelli, E. 2003, MNRAS, 342, 199

Corbelli, E., Lorenzoni, S., Walterbos, R., Braun, R., & Thilker, D. 2010, A&A, 511, A89
Corbelli, E., & Salucci, P. 2000, MNRAS, 311, 441
Corbelli, E., & Schneider, S. E. 1997, ApJ, 479, 244
Cosens, M., Wright, S. A., Sandstrom, K., et al. 2024, AJ, 168, 250
Dalcanton, J. J., Williams, B. F., Melbourne, J. L., et al. 2012, ApJS, 198, 6
Dame, T. M., Koper, E., Israel, F. P., & Thaddeus, P. 1993, ApJ, 418, 730
Dawson, J. R., Breen, S. L. & Gaskap-Oh Team. 2024, in IAU Symp. 380, Cosmic Masers: Proper Motion Toward the Next-Generation Large Projects, ed. T. Hirota et al. (Cambridge: Cambridge Univ. Press), 486
de Blok, W. J. G., Healy, J., Maccagni, F. M., et al. 2024, A&A, 688, A109
de Blok, W. J. G., & Walter, F. 2006, AJ, 131, 343
Dell'Agli, F., Di Criscienzo, M., Ventura, P., et al. 2018, MNRAS, 479, 5035
Deul, E. R., & van der Hulst, J. M. 1987, A&AS, 67, 509
Dickel, J. R., Dodorico, S., & Silverman, A. 1985, AJ, 90, 414
Dickey, J. M., McClure-Griffiths, N., Gibson, S. J., et al. 2013, PASA, 30, e003
Dobbs, C. L., Krumholz, M. R., Ballesteros-Paredes, J., et al. 2014, in Protostars and Planets VI, ed. H. Beuther et al. (Tucson, AZ: Univ. Arizona Press), 3
Draine, B. T., Aniano, G., Krause, O., et al. 2014, ApJ, 780, 172
Elmegreen, B. G., Palouš, J., & Ehlerová, S. 2002, MNRAS, 334, 693
Elmegreen, B. G., & Scalo, J. 2004, ARA&A, 42, 211
Ewen, H. I., & Purcell, E. M. 1951, Natur, 168, 356
Ferrière, K. M. 2001, RvMP, 73, 1031
Field, G. B. 1958, PIRE, 46, 240
Flaugher, B., Diehl, H. T., Honscheid, K., et al. 2015, AJ, 150, 150
Fraternali, F. 2017, in Gas Accretion onto Galaxies, ed. A. Fox & R. Davé, Vol. 430 (Berlin: Springer), 323
Gerbrandt, S. A. N., McConnachie, A. W., & Irwin, M. 2015, MNRAS, 454, 1000
Ginsburg, A., Giessel, A., & Chef, B. 2014, image_registration v0.2.1, Zenodo, doi:10.5281/zenodo.12528
Ginsburg, A., Koch, E., Robitaille, T., et al. 2019, radio-astro-tools/spectral-cube: Release v0.4.5, Zenodo, doi:10.5281/zenodo.3558614
Gratier, P., Braine, J., Rodriguez-Fernandez, N. J., et al. 2010a, A&A, 512, A68
Gratier, P., Braine, J., Rodriguez-Fernandez, N. J., et al. 2010b, A&A, 522, A3
Gray, M. D., Howe, D. A., & Lewis, B. M. 2005, MNRAS, 364, 783
Hacar, A., Clark, S. E., Heitsch, F., et al. 2023, in ASP Conf. Ser. 534, Protostars and Planets VII, ed. S. Inutsuka et al. (San Francisco, CA: ASP), 153
Heald, G., Józsa, G., Serra, P., et al. 2011, A&A, 526, A118
Heiles, C., & Troland, T. H. 2003, ApJ, 586, 1067
Holtzman, J. A., Afonso, C., & Dolphin, A. 2006, ApJS, 166, 534
Hunt, L. K., Annibali, F., Cuillandre, J. C., et al. 2025, A&A, 697, A9
Hunter, D. A. 2001, ApJ, 559, 225
Hunter, D. A., Elmegreen, B. G., & Madden, S. C. 2024, ARA&A, 62, 113
Hunter, D. A., Ficut-Vicas, D., Ashley, T., et al. 2012, AJ, 144, 134
Hunter, D. A., Zahedy, F., Bowsher, E. C., et al. 2011, AJ, 142, 173
Hunter, J. D. 2007, CSE, 9, 90
Ianjamasimanana, R., Namumba, B., Ramaila, A. J. T., et al. 2020, MNRAS, 497, 4795
Jackson, D. C., Skillman, E. D., Cannon, J. M., & Côté, S. 2004, AJ, 128, 1219
Jarrett, T. H., Chester, T., Cutri, R., Schneider, S. E., & Huchra, J. P. 2003, AJ, 125, 525
Johnson, M. 2013, AJ, 145, 146
Jones, O. C., Boyer, M. L., McDonald, I., Meixner, M., & van Loon, J. T. 2023, MNRAS, 525, 3693
Joshi, Y. C., Sharma, K., Gangopadhyay, A., Gokhale, R., & Misra, K. 2019, AJ, 158, 175
Kam, S. Z., Carignan, C., Chemin, L., et al. 2017, AJ, 154, 41
Karachentsev, I. D., Karachentseva, V. E., Huchtmeier, W. K., & Makarov, D. I. 2004, AJ, 127, 2031
Karachentsev, I. D., Makarov, D. I., & Kaisina, E. I. 2013, AJ, 145, 101
Keenan, O. C., Davies, J. I., Taylor, R., & Minchin, R. F. 2016, MNRAS, 456, 951
Kepley, A. A., Wilcots, E. M., Hunter, D. A., & Nordgren, T. 2007, AJ, 133, 2242
Kerr, F. J., Hindman, J. F., & Robinson, B. J. 1954, AuJPh, 7, 297
Koch, E., & Ginsburg, A., 2022 uvcombine: Combine Images with Different Resolutions, Astrophysics Source Code Library, ascl:2208.014
Koch, E., Rosolowsky, E., Johnson, M. C., Kepley, A. A., & Leroy, A. 2018a, RNAAS, 2, 24
Koch, E. W., Chiang, I.-D., Utomo, D., et al. 2020, MNRAS, 492, 2663
Koch, E. W., Rosolowsky, E. W., Leroy, A. K., et al. 2021, MNRAS, 504, 1801
Koch, E. W., Rosolowsky, E. W., Lockman, F. J., et al. 2018b, MNRAS, 479, 2505
Koribalski, B. S., Wang, J., Kamphuis, P., et al. 2018, MNRAS, 478, 1611
Krumholz, M. R. 2014, PhR, 539, 49
Krumholz, M. R., Leroy, A. K., & McKee, C. F. 2011, ApJ, 731, 25
Lake, G., & Skillman, E. D. 1989, AJ, 98, 1274
Law, C. J., Bower, G. C., Burke-Spolaor, S., et al. 2018, ApJS, 236, 8
Lee, A. J., Freedman, W. L., Madore, B. F., et al. 2021, ApJ, 907, 112
Lee, A. J., Monson, A. J., Freedman, W. L., et al. 2024, ApJ, 967, 22
Lee, H., Skillman, E. D., & Venn, K. A. 2005, ApJ, 620, 223
Lee, H., Skillman, E. D., & Venn, K. A. 2006, ApJ, 642, 813
Lee, J. H., & Lee, M. G. 2014, ApJ, 786, 130
Leroy, A., Bolatto, A., Walter, F., & Blitz, L. 2006, ApJ, 643, 825
Leroy, A. K., Hughes, A., Liu, D., et al. 2021, ApJS, 255, 19
Leroy, A. K., Sandstrom, K. M., Lang, D., et al. 2019, ApJS, 244, 24
Leroy, A. K., Walter, F., Brinks, E., et al. 2008, AJ, 136, 2782
Licquia, T. C., & Newman, J. A. 2015, ApJ, 806, 96
Lockett, P., Gauthier, E., & Elitzur, M. 1999, ApJ, 511, 235
Lockman, F. J., Free, N. L., & Shields, J. C. 2012, AJ, 144, 52
Lozinskaya, T. A., & Podorvanyuk, N. Y. 2009, AstL, 35, 375
Lucchini, S., D'Onghia, E., & Fox, A. J. 2021, ApJL, 921, L36
Mac Low, M.-M., & Klessen, R. S. 2004, RvMP, 76, 125
Maccagni, F. M., & de Blok, W. J. G. 2024, arXiv:2407.03166
Makarov, D., Prugniel, P., Terekhova, N., Courtois, H., & Vauglin, I. 2014, A&A, 570, A13
Marganian, P., Garwood, R. W., Braatz, J. A., Radziwill, N. M., & Maddalena, R. J., 2013 GBTIDL: Reduction and Analysis of GBT Spectral Line Data, Astrophysics Source Code Library, ascl:1303.019
Mateo, M. L. 1998, ARA&A, 36, 435
McClure-Griffiths, N. M., Stanimirović, S., & Rybarczyk, D. R. 2023, ARA&A, 61, 19
McConnachie, A. W. 2012, AJ, 144, 4
Mittal, A. K., Babler, B. L., Stanimirović, S., & Pingel, N. 2023, ApJ, 958, 192
Morganson, E., Gruendl, R. A., Menanteau, F., et al. 2018, PASP, 130, 074501
Muraoka, K., Konishi, A., Tokuda, K., et al. 2023, ApJ, 953, 164
Murphy, E. J., Bolatto, A., Chatterjee, S., et al. 2018, in ASP Conf. Ser. 517, Science with a Next Generation Very Large Array, ed. E. Murphy (San Francisco, CA: ASP), 3
Murray, C. E., Lindner, R. R., Stanimirović, S., et al. 2014, ApJL, 781, L41
Murray, C. E., Stanimirović, S., Goss, W. M., et al. 2018, ApJS, 238, 14
Murray, C. E., Stanimirović, S., Goss, W. M., et al. 2015, ApJ, 804, 89
Namumba, B., Carignan, C., Foster, T., & Deg, N. 2019, MNRAS, 490, 3365
Namumba, B., Carignan, C., Passmoor, S., & de Blok, W. J. G. 2017, MNRAS, 472, 3761
Nidever, D. L., Ashley, T., Slater, C. T., et al. 2013, ApJL, 779, L15
Nieten, C., Neininger, N., Guélin, M., et al. 2006, A&A, 453, 459
Oh, S.-H., Hunter, D. A., Brinks, E., et al. 2015, AJ, 149, 180
Ohta, K., Tomita, A., Saito, M., Sasaki, M., & Nakai, N. 1993, PASJ, 45, L21
Ott, J., Stilp, A. M., Warren, S. R., et al. 2012, AJ, 144, 123
Padmanabh, P. V., Barr, E. D., Sridhar, S. S., et al. 2023, MNRAS, 524, 1291
Park, H.-J., Oh, S.-H., Wang, J., et al. 2022, AJ, 164, 82
Paturel, G., Petit, C., Prugniel, P., et al. 2003, A&A, 412, 45
Peek, J. E. G., Heiles, C., Douglas, K. A., et al. 2011, ApJS, 194, 20
Peltonen, J., Rosolowsky, E., Williams, T. G., et al. 2024, MNRAS, 527, 10668
Perley, R. A., & Butler, B. J. 2017, ApJS, 230, 7
Perley, R. A., Chandler, C. J., Butler, B. J., & Wrobel, J. M. 2011, ApJL, 739, L1
Pingel, N. M., Chen, H., Stanimirović, S., et al. 2024, ApJ, 974, 93
Pingel, N. M., Dempsey, J., McClure-Griffiths, N. M., et al. 2022, PASA, 39, e005
Pingel, N. M., Pisano, D. J., Heald, G., et al. 2018, ApJ, 865, 36
Putman, M. E., Peek, J. E. G., & Joung, M. R. 2012, ARA&A, 50, 491
Putman, M. E., Peek, J. E. G., Muratov, A., et al. 2009, ApJ, 703, 1486
Putman, M. E., Staveley-Smith, L., Freeman, K. C., Gibson, B. K., & Barnes, D. G. 2003, ApJ, 586, 170
Putman, M. E., Zheng, Y., Price-Whelan, A. M., et al. 2021, ApJ, 913, 53
Rémy-Ruyer, A., Madden, S. C., Galliano, F., et al. 2014, A&A, 563, A31
Rogers, N. S. J., Skillman, E. D., Pogge, R. W., et al. 2022, ApJ, 939, 44
Rubio, M., Elmegreen, B. G., Hunter, D. A., et al. 2015, Natur, 525, 218
Saintonge, A., & Catinella, B. 2022, ARA&A, 60, 319
Sancisi, R., Fraternali, F., Oosterloo, T., & van der Hulst, T. 2008, A&ARv, 15, 189
Sanna, N., Bono, G., Stetson, P. B., et al. 2008, ApJL, 688, L69

Sardone, A., Pisano, D. J., Pingel, N. M., et al. 2021, ApJ, 910, 69
Sasaki, M., Pietsch, W., Haberl, F., et al. 2012, A&A, 544, A144
Savino, A., Weisz, D. R., Skillman, E. D., et al. 2022, ApJ, 938, 101
Saydjari, A. K., & Finkbeiner, D. P. 2022, ApJ, 933, 155
Schinnerer, E., & Leroy, A. K. 2024, ARA&A, 62, 369
Schruba, A., Leroy, A. K., Walter, F., et al. 2011, AJ, 142, 37
Schruba, A., Leroy, A. K., Kruijssen, J. M. D., et al. 2017, ApJ, 835, 278
Shostak, G. S., & Skillman, E. D. 1989, A&A, 214, 33
Silich, S., Lozinskaya, T., Moiseev, A., et al. 2006, A&A, 448, 123
Stanimirovic, S., Staveley-Smith, L., Dickey, J. M., Sault, R. J., & Snowden, S. L. 1999, MNRAS, 302, 417
Steer, I., Madore, B. F., Mazzarella, J. M., et al. 2017, AJ, 153, 37
Sternberg, A., Le Petit, F., Roueff, E., & Le Bourlot, J. 2014, ApJ, 790, 10
Sun, J., Leroy, A. K., Rosolowsky, E., et al. 2022, AJ, 164, 43
Sun, J., Leroy, A. K., Schruba, A., et al. 2018, ApJ, 860, 172
Tabatabaei, F. S., Beck, R., Krügel, E., et al. 2007, A&A, 475, 133
Tabatabaei, F. S., Cotton, W., Schinnerer, E., et al. 2022, MNRAS, 517, 2990
Tacconi, L. J., Genzel, R., & Sternberg, A. 2020, ARA&A, 58, 157
Telford, O. G., Dalcanton, J. J., Williams, B. F., et al. 2020, ApJ, 891, 32
Thilker, D. A., Braun, R., & Walterbos, R. A. M. 2002, in ASP Conf. Ser. 276, Seeing Through the Dust: The Detection of HI and the Exploration of the ISM in Galaxies, ed. A. R. Taylor, T. L. Landecker, & A. G. Willis (San Francisco, CA: ASP), 370
Thilker, D. A., Braun, R., Walterbos, R. A. M., et al. 2004, ApJL, 601, L39
Thompson, T. A., & Heckman, T. M. 2024, ARA&A, 62, 529
Utomo, D., Blitz, L., & Falgarone, E. 2019, ApJ, 871, 17
van de Hulst, H. C. 1945, Nederlandsch Tijdschrift voor Natuurkunde, 11, 210
van den Bergh, S. 1999, A&ARv, 9, 273
Virtanen, P., Gommers, R., Oliphant, T. E., et al. 2020, NatMe, 17, 261
Walter, F., Brinks, E., de Blok, W. J. G., et al. 2008, AJ, 136, 2563
Walter, F., Carilli, C., Neeleman, M., et al. 2020, ApJ, 902, 111
Wang, J., Koribalski, B. S., Serra, P., et al. 2016, MNRAS, 460, 2143
Waskom, M., Botvinnik, O., O'Kane, D., et al. 2017, mwaskom/seaborn: v0.8.1, Zenodo, doi:10.5281/zenodo.883859
Weisz, D. R., Dolphin, A. E., Savino, A., et al. 2024, ApJS, 271, 47
Weldrake, D. T. F., de Blok, W. J. G., & Walter, F. 2003, MNRAS, 340, 12
Westcott, J., Brinks, E., Beswick, R. J., et al. 2017, MNRAS, 467, 2113
Westmeier, T., Braun, R., & Thilker, D. 2005, A&A, 436, 101
White, R. L., Long, K. S., Becker, R. H., et al. 2019, ApJS, 241, 37
Wilcots, E. M., & Miller, B. W. 1998, AJ, 116, 2363
Williams, B. F., Durbin, M. J., Dalcanton, J. J., et al. 2021, ApJS, 253, 53
Wolfire, M. G., Vallini, L., & Chevance, M. 2022, ARA&A, 60, 247
Yang, H., & Skillman, E. D. 1993, AJ, 106, 1448
Yang, Y., Ianjamasimanana, R., Hammer, F., et al. 2022, A&A, 660, L11
Yin, J., Hou, J. L., Prantzos, N., et al. 2009, A&A, 505, 497
Zurita, A., & Bresolin, F. 2012, MNRAS, 427, 1463